



HAL
open science

A 4.5 Year-Long Record of Svalbard Water Vapor Isotopic Composition Documents Winter Air Mass Origin

C. Leroy-dos Santos, V. Masson-delmotte, M. Casado, E. Fourré, H. Steen-larsen, M. Maturilli, A. Orsi, A. Berchet, O. Cattani, B. Minster, et al.

► **To cite this version:**

C. Leroy-dos Santos, V. Masson-delmotte, M. Casado, E. Fourré, H. Steen-larsen, et al.. A 4.5 Year-Long Record of Svalbard Water Vapor Isotopic Composition Documents Winter Air Mass Origin. *Journal of Geophysical Research: Atmospheres*, 2020, 125 (23), 10.1029/2020JD032681 . hal-03087623

HAL Id: hal-03087623

<https://hal.science/hal-03087623v1>

Submitted on 22 Feb 2021

HAL is a multi-disciplinary open access archive for the deposit and dissemination of scientific research documents, whether they are published or not. The documents may come from teaching and research institutions in France or abroad, or from public or private research centers.

L'archive ouverte pluridisciplinaire **HAL**, est destinée au dépôt et à la diffusion de documents scientifiques de niveau recherche, publiés ou non, émanant des établissements d'enseignement et de recherche français ou étrangers, des laboratoires publics ou privés.

25 Abstract

26 From May 2014 to September 2018, a laser spectrometer analyzer provided a 4.5 years
27 continuous record of water vapor isotopic composition at Ny-Ålesund (8 m a.s.l.), Svalbard. It
28 corresponds to the longest dataset published in polar regions. A comparison of this dataset with
29 a parallel similar dataset obtained during 20 days by a second laser spectrometer installed at the
30 near Mount Zeppelin (474 m a.s.l.) shows that this dataset is representative of a regional signal.
31 In addition, the observation of insignificant diurnal cycles in the isotopic signal compared to
32 the strong isotopic signature of synoptic events and the comparison of simultaneous
33 measurements in the vapor and in rain or snow samples lead to the conclusion that our record
34 reflects a large part of the regional dynamics of the atmospheric water cycle driven by large
35 scale variability. This study focuses on winters dominated by the occurrence of synoptic events
36 associated with humidity peaks. Using statistics and back-trajectories calculations, we link high
37 humidity peaks characterized by an anti-correlation between $\delta^{18}\text{O}$ and d-excess in the water
38 vapor to a rapid shift of air mass source regions from the Arctic to the North Atlantic Ocean
39 below 60°N . On the other hand, correlation between $\delta^{18}\text{O}$ and d-excess may be associated with
40 a shift of air mass sources within the Arctic. These results demonstrate the added value of long-
41 term water vapor isotopic monitoring to better understand the moisture origin in the Arctic and
42 the atmospheric dynamics.

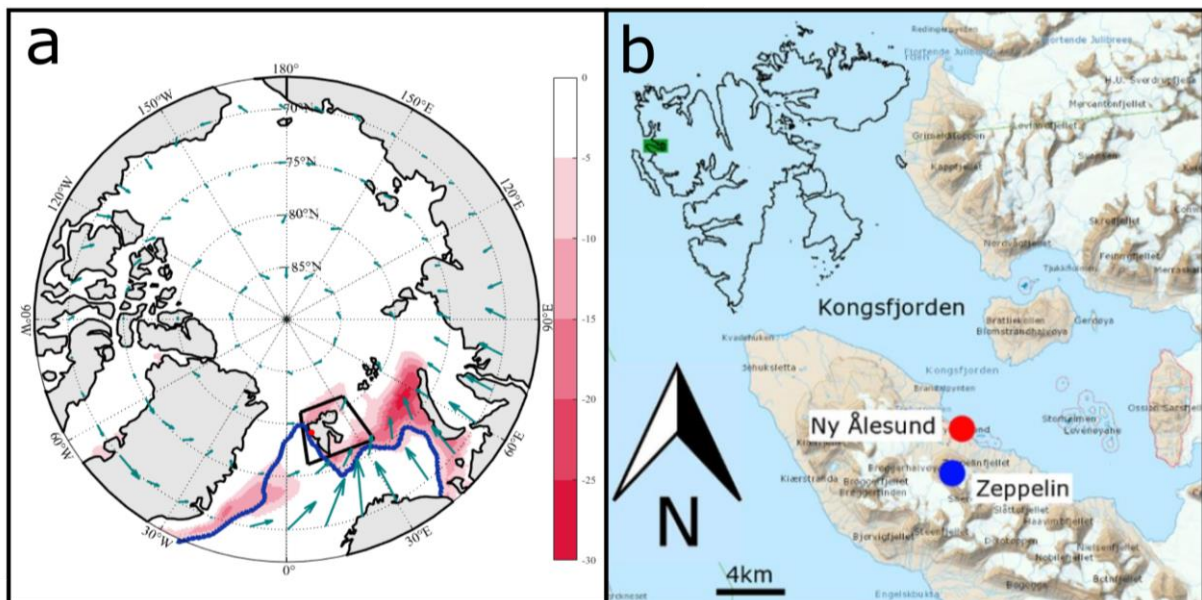
43

44 1. Introduction

45 In the current context of climate change, the Arctic region is specifically under focus because
46 of the extreme high temperatures and low sea ice extents observed over recent years (Arctic
47 Monitoring and Assessment Programme, 2017; Meredith et al., 2019; Overland & Wang, 2018;
48 Walsh et al., 2017). The long-term increase in annual temperature in the Arctic region is 2-3
49 times larger than the global average (Gjelten et al., 2016), due to a number of polar amplification
50 processes involving changes in albedo, water vapor, summer cloudiness, the presence of open
51 water in autumn, but also the transport of heat and moisture associated with the intrusion of
52 sub-arctic storms (Goosse et al., 2018; Meredith et al., 2019; Screen & Simmonds, 2010).
53 Linked to atmospheric circulation patterns, recent studies also highlighted the occurrence of
54 “atmospheric rivers” as an important modulation of the moisture transport to the Arctic region
55 (Alekseev et al., 2019; Bonne et al., 2015; Hao et al., 2019; Liu & Barnes, 2015; Naakka et al.,
56 2019; Woods et al., 2013).

57 Seasonally surrounded by sea ice, Svalbard stands at the intersection between cold polar air
 58 travelling from the north and oceanic air travelling from the south (Figure 1). Svalbard is hence
 59 at a key location to study changes of the atmospheric water cycle organization in the Arctic
 60 region, which is key to gain a better understanding of the role of sea ice extent variations on the
 61 Arctic climate processes (Ding et al., 2017) since recent sea ice decline leads to an increase of
 62 local evaporation sources (Dufour et al., 2016). Due to its geographic position, Svalbard climate
 63 evolution is strongly affected by Arctic amplification (warming at a rate of $0.8 \pm 0.2 \text{ }^\circ\text{C.decade}^{-1}$
 64 ¹ on the 1979-2019 period (Figure S1 and Text S1) and is influenced by regional processes
 65 controlling sea ice variations and moisture transport from the North Atlantic sector (Dahlke et
 66 al., 2020; Hanssen-Bauer & Førland, 1998; Isaksen et al., 2016; Rinke et al., 2017).

67 A robust signal in climate projections is the increasing trend of Arctic precipitation by the end
 68 of the 21st century, but climate models show a large dispersion in the relative contributions of
 69 local recycling and enhanced advection to this increase in precipitation amount (Bintanja &
 70 Selten, 2014). Two main effects are expected to influence the moisture content in the Svalbard
 71 region: evaporation over the ocean (Dufour et al., 2016) and atmospheric circulation patterns
 72 leading to moisture transport from Atlantic, Arctic or continental regions (Dahlke & Maturilli,
 73 2017; Vázquez et al., 2016). This motivates the exploration of the air mass origin signal
 74 captured by water stable isotopes in Svalbard water vapor and precipitation in this study.



75
 76 *Figure 1. a) Linear trend (% per decade) of winter maximum sea-ice concentration from ERA-*
 77 *5 reanalyses (over the 1979-2018 period) in pink; mean-sea ice extent in March (blue line);*
 78 *integrated horizontal vapor fluxes (DJF) are plotted on some grid points (green arrow lengths*

79 *are proportional to vapor flux in $\text{kg}\cdot\text{m}^{-1}\cdot\text{s}^{-1}$). The area delineated by the black line corresponds*
80 *to ERA 5 selected grid points used in supporting information Figure S1. b) Map of*
81 *Kongsfjorden, Svalbard (modified from Eckhardt et al. (2013)): Ny-Ålesund (8 m a.s.l.) and*
82 *Zeppelin (474 m a.s.l.).*

83 Water stable isotopes are a classical tool to study the organization of the atmospheric water
84 cycle (Gat, 1996; Jouzel, 2003). We use the δ notation to express the ratio (in per mil, ‰)
85 between heavier (HD^{16}O or H_2^{18}O) molecules and lighter molecules (H_2^{16}O):
86 $\delta = (\text{R}_{\text{sample}}/\text{R}_{\text{VSMOW}} - 1) \cdot 1000$ where R_{sample} is the ratio between heavier and lighter water
87 molecules of measured sample and R_{VSMOW} is the ratio between heavier and lighter water
88 molecules of the reference water (Vienna Standard Mean Ocean Water). In polar continental
89 regions such as Greenland or the East Antarctic plateau, $\delta^{18}\text{O}$ and δD are closely controlled by
90 changes in temperature along the trajectory from the warm regions of evaporation to the polar
91 regions leading to a distillation process and thus a decrease in the heavy isotope content in
92 atmospheric water vapor (Jouzel et al., 2013; Masson-Delmotte et al., 2008). In addition, the
93 second-order parameter, d-excess ($\text{d-excess} = \delta\text{D} - 8 \cdot \delta^{18}\text{O}$, Dansgaard, 1964) brings
94 complementary information on the climatic conditions of the source evaporative region and
95 moisture recycling over the distillation path. Variations in d-excess result from different
96 sensitivities of δD and $\delta^{18}\text{O}$ to kinetic fractionation processes such as diffusion during
97 evaporation and moisture uptake occurring along the atmospheric transport pathway (Craig &
98 Gordon, 1965). During evaporation over the ocean, high (low) relative humidity levels lead to
99 small (high) kinetic fractionation hence low (high) d-excess. The combination of $\delta^{18}\text{O}$ and δD
100 can thus provide quantitative insights on the origin and dynamics of moisture trajectories.
101 Bonne et al. (2014) have shown that this initial d-excess signal is partially preserved during
102 moisture transport towards Greenland. During snow formation, kinetic effects are also at play,
103 especially for situation of high supersaturation, and they affect the d-excess values in polar
104 regions (Jouzel & Merlivat, 1984).

105 Until recently, water isotopes measurements were only possible on the condensed phase, hence
106 limiting their use to the study of atmospheric water cycle of rain and snowfall events. Some early
107 studies performed water vapor analyses by trapping water vapor in a cold trap for several hours
108 to get sufficient water for liquid analyses (Angert et al., 2004; Steen-Larsen et al., 2011). The
109 recent progress of optical spectroscopy now permits the continuous measurement with high
110 accuracy of the water vapor isotopic composition (Aemisegger et al., 2012; Galewsky et al.,
111 2016; Tremoy et al., 2011). This new ability to monitor continuously δD and $\delta^{18}\text{O}$ of the water

112 vapor has been implemented during several measurement campaigns in different Arctic
113 environments: over the Greenland ice sheet in summer (Berkelhammer et al., 2016; Steen-
114 Larsen et al., 2013, 2014), in the marine boundary layer during oceanic campaigns on research
115 vessels (Benetti et al., 2017; Bonne et al., 2019), as at coastal sites (Bonne et al., 2014; Kopec
116 et al., 2014; Steen-Larsen et al., 2015), or in more continental and vegetated area like Siberia
117 (Bastrikov et al., 2014). While being very useful to characterize the water cycle dynamics over
118 a period in the region of interest, there are some limitations in the series already available. For
119 example, none of the aforementioned records exceeds 12 consecutive months of monitoring at
120 the same place, while at least 24 months would be needed to study interannual variations of the
121 vapor isotopic composition.

122 With the aim to study the changes of origin of moisture trajectories to the Arctic region and the
123 link with synoptic variability at seasonal and interannual scales, we installed a laser
124 spectroscopy instrument to monitor the evolution of $\delta^{18}\text{O}$ and δD at Ny-Ålesund AWIPEV
125 station, Svalbard (8 m a.s.l., Figure 1). It results in the longest time series record of water vapor
126 stable isotopic composition (4.5 years), a period characterized by the highest mean annual
127 temperature over the 1979-2018 period (-1.1°C in 2016) and by a low sea ice extent, as shown
128 in Figure S1. This record has been completed with a comparison to measurements of water
129 vapor isotopic composition at the neighbor site of Mount Zeppelin (474 m a.s.l.). Additionally,
130 meteoric water samples were recovered at Ny-Ålesund AWIPEV station during each
131 precipitation event, rainfall or snowfall.

132 This paper is organized into three sections. In section 2, we present the methods used to obtain,
133 calibrate and validate the 4.5-year records of water isotopic composition in vapor and in
134 precipitation, as well as meteorological data at the study site and methods to retrieve 5-day back
135 trajectories. Section 3 presents the full dataset. Section 4 focuses on the information brought by
136 water isotopes to document the origin of moisture arriving to Svalbard during winter humidity
137 peaks.

138

139 **2. Data and Methods**

140 **2.1. Meteorological data**

141 Meteorological data are available since 1993 at the AWIPEV observatory (Maturilli, 2020a).
142 Hereafter, we use the 2-meter air temperature ($^\circ\text{C}$), the specific humidity (volume mixing ratio
143 in ppmv), the cloud base (CLB) height (m) (Maturilli & Ebell, 2018) and the radiosonde

144 measurements (Maturilli, 2018, 2020b) from Ny-Ålesund station provided by the Alfred
145 Wegener Institute – Research Unit Potsdam.

146

147 We also use outputs from the global atmospheric reanalysis of the European Center for
148 Medium-Range Weather Forecasts (ECMWF), ERA-5 6-hourly averaged data on pressure
149 levels from 1979 to 2018: the total daily precipitation amount (m), the sea ice area fraction, the
150 vertical integral of the water vapor flux ($\text{kg} \cdot \text{m}^{-1} \cdot \text{s}^{-1}$) and the temperature ($^{\circ}\text{C}$).

151

152 **2.2. Water vapor monitoring**

153

154 Two Picarro laser spectrometer instruments based on the cavity ring-down spectroscopy
155 (CRDS) technique were installed in Ny-Ålesund (8 m above sea level), in the AWIPEV
156 observatory building (Figure S3; Text S3): a L1102-i Picarro instrument from May 2014 to
157 May 2015 and then a L2130-i Picarro instrument until the end of the measurement campaign
158 (27/09/2018). The change of instrument is justified by the enhanced performances of the more
159 recent L2130-i Picarro (precision of 0.1 ‰ and 0.8 ‰ for $\delta^{18}\text{O}$ and δD respectively, 30 second
160 injection at 2500 ppmv, measurement rate of 1 Hz) compared to the L1102-i Picarro (precision
161 of 0.2 ‰ and 1 ‰ for $\delta^{18}\text{O}$ and δD respectively, 30 second injection at 10000 ppmv,
162 measurement rate of 0.1 Hz) (Picarro Inc., 2009, 2016). The outside air was continuously
163 pumped through a heated sampling line installed along the building, with an inlet located 10 m
164 above the ground level. The instrumental transition occurred in two phases: first, the L2130-i
165 instrument was installed at Zeppelin observatory (474 m a.s.l., 1.2 km from Ny-Ålesund) and
166 operated in parallel with the L1102-i instrument at Ny-Ålesund during two weeks (06/05/2015
167 to 23/05/2015, Figure S4). It was then set up at Ny-Ålesund (8 m a.s.l.) to replace the L1102-i
168 instrument. The full data series at Ny-Ålesund (Figure 2) presents some missing measurements:
169 1) every day, 2 hours were dedicated to standard measurements for calibration; 2) some longer
170 periods (e.g. from 23/04/2016 to 11/05/2016) were dedicated to the maintenance of the set-up.

171

172 The raw data from the CRDS instruments need to be calibrated as discussed previously in
173 several publications to ensure consistency with the international VSMOW-SLAP scale
174 (International Atomic Energy Agency, 2006). The volume water vapor mixing ratio in ppmv,
175 hereafter referred to as humidity, is continuously measured by the CRDS instrument. A
176 multiplying correction factor (0.91 and 1.02 respectively for our L1102-i and L2130-i

177 instruments) is applied to the measured humidity in order to match the local meteorological
178 data from AWIPEV (Figure S5, Text S4 and Text S5).

179

180 Following the protocol outlined in previous publications (Bonne et al., 2014; Steen-Larsen et
181 al., 2014; Tremoy et al., 2011), three main corrections are applied to the isotopic data to account
182 for: 1) the influence of humidity on $\delta^{18}\text{O}$ and δD measurement (Text S6), 2) the shift between
183 the measured values and the true isotopic values (Text S7), and 3) the temporal drift of the
184 instrument (Text S7), which refers to the temporal evolution of the shift between measured and
185 true values (Figure S6). The calibration set-up introduces vapor into the instrument with a
186 known isotopic composition at prescribed humidity levels (Text S4). The influence of humidity
187 on water vapor isotopic composition is determined during 2 calibration campaigns through a
188 series of measurements of water isotopic standard injected at different humidity levels (Figure
189 S7).

190 The isotope-humidity calibration determined for the second instrument is unfortunately more
191 scattered than for the first instrument below 2000 ppmv. It nevertheless shows that, above 2000
192 ppmv, the isotope vs humidity correction is small ($< 0.1\text{‰}$ and $< 0.3 \text{‰}$ for $\delta^{18}\text{O}$ and δD ,
193 respectively). The mean standard deviation is 1.3 ‰ (6.5 ‰) for $\delta^{18}\text{O}$ (δD) for measurements
194 performed at humidity levels lower than 2000 ppmv and 0.4‰ (1.4‰) for $\delta^{18}\text{O}$ (δD)
195 measurement performed at humidity levels higher than 2000 ppmv (Text S6 and Figures S6 and
196 S7). This study will thus focus on winter periods during which humidity values are higher than
197 2000 ppmv.

198

199 The other two corrections are calculated by measuring two water isotopic standards with
200 isotopic values bracketing the measured values at least once a day at constant humidity level
201 (set at 3700 ppmv between May 2014 and December 2016 and then at 6900 ppmv for the rest
202 of the campaign) (Texts S4, S7 and Figure S6). The uncertainty on the water vapor isotopic
203 data can then be calculated from the instrument replication (internal accuracy) and the
204 uncertainties associated with these corrections (Text S8, Figures S8, S9 and S10).

205

206 When the calibration system is working adequately (79% of the time), the uncertainty only due
207 to the reproducibility of daily standard measurements (including internal accuracy and
208 uncertainty on the drift of the instrument) is estimated to 0.11 ‰ for $\delta^{18}\text{O}$ and 0.70 ‰ for δD .
209 When no daily calibration is available (21% of the time), this uncertainty rises up to 0.18 ‰ for

210 $\delta^{18}\text{O}$ and 1.38 ‰ for δD . This uncertainty does not take into account possible biases due to
211 variation of the influence of humidity on water vapor isotopic composition which is expected
212 to be constant over the whole period of measurements according to our measurements (Text S6
213 and Figure S7) and previous study (Bailey et al., 2015).

214

215 **2.3. Precipitation monitoring**

216

217 Whenever precipitation events occurred, water or snow was sampled daily at midday and stored
218 in a glass container at 8-10°C and shipped to LSCE for measurement. Altogether, 519 samples
219 were collected over the 4.5 years. Samples were sent back to LSCE every 6 months. Water
220 stable isotope measurements were performed with a Picarro CRDS instrument working in liquid
221 mode, i.e. with vaporization of the samples in dry air to reach a humidity of 20,000 ppmv.
222 Replicates were performed over 15% of the samples so that we could calculate the uncertainty
223 (2σ) for our dataset to 0.05 ‰ and 0.2 ‰ respectively for $\delta^{18}\text{O}$ and δD .

224

225 **2.4. Back-trajectories**

226

227 The origin and trajectory of air masses were evaluated using the HYSPLIT model (Hybrid-
228 Single Particle Lagrangian Integrated Trajectory) (Stein et al., 2015;
229 http://ready.arl.noaa.gov/HYSPLIT_traj.php). In this model, the position of the air mass is
230 determined using a three-dimensional Lagrangian air mass vertical velocity algorithm. The set
231 of meteorological data used to simulate trajectories was taken from ERA-5. We have calculated
232 5 days back-trajectories with a single launch of one particle every 6 hours at 500 m.a.s.l. above
233 Ny-Ålesund coordinates throughout the full data series period. Hysplit was used here to provide
234 an estimate of the origin of air masses over specific moist events from our 4.5 years' dataset.
235 We have chosen a 500 m.a.s.l altitude for the particle launch for several reasons. First, the
236 vertical mixing in HYSPLIT is not ideally represented (Ngan et al., 2019) so that we expect
237 artefacts when running the particle launch at 10 m.a.s.l. (where the inlet was actually located).
238 Second, we checked that the temporal evolution of the water vapor isotopic composition is the
239 same at 10 m.a.s.l. and 500 m.a.s.l. (section 3.4). Finally, a sensitivity test has been performed
240 comparing back-trajectories at 500 m.a.s.l. and 10 m.a.s.l. on a 2-year period (June 2014 to
241 September 2016) :only 20 back-trajectories over 308 have opposite origin when comparing
242 those obtained from a launch of particles at 500 m.a.s.l. to those obtained from a launch of
243 particles at 10 m.a.s.l. Despite being convenient to produce diagnostics over long-time series,

244 Hysplit has however some limitations. As Hysplit computations are based on single particle
245 trajectories, the representativeness of our estimates might not be correct. To assess this point,
246 we used in addition to Hysplit the Lagrangian Particle Dispersion Model Flexpart (Stohl et al.,
247 2005) with a large ensemble of particles for a couple of selected events: every 6 hours a batch
248 of 500 neutral inert air tracer particles are randomly released from a volume ($0.1^\circ \times 0.1^\circ \times 100$ m)
249 centered around Ny-Ålesund coordinates (at an altitude of 50 m.a.s.l). Flexpart is driven by
250 meteorological fields from ERA5 to compute 10-day back-trajectories. We developed
251 visualization tools to display the concentration of particles being transported above each grid
252 point in latitude-longitude and latitude-altitude maps (Text S9).

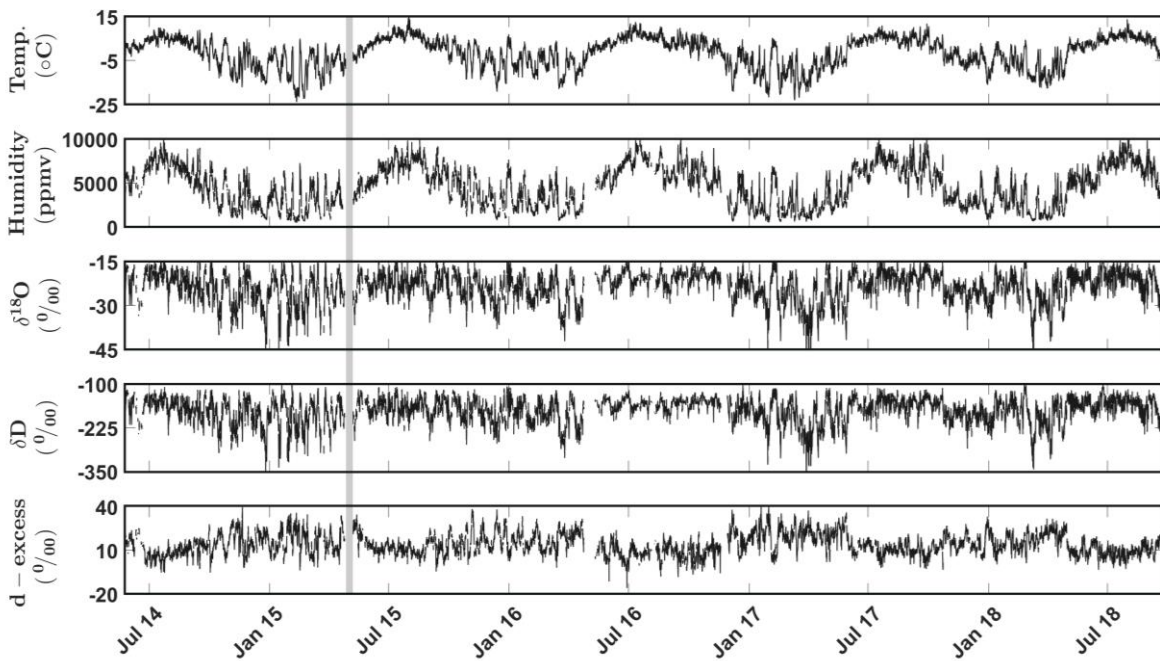
253 **3. Results**

254 In this section, we first present the full 4.5-year data set at Ny-Ålesund for the water vapor
 255 isotopic composition as well as its variability at the inter-annual, seasonal and diurnal scale.
 256 This data set is then compared to the short series of parallel measurements of the water vapor
 257 at the nearby site of Mount Zeppelin (474 m a.s.l.), and finally to the 4.5 years' record of
 258 meteoric water isotopic composition sampled at the event scale at Ny-Ålesund.

259

260 **3.1 Isotopic composition of the vapor water at Ny-Ålesund and links with meteorological**
 261 **data**

262 The full calibrated hourly data series spanning 4.5 years are displayed in Figure 2.



263

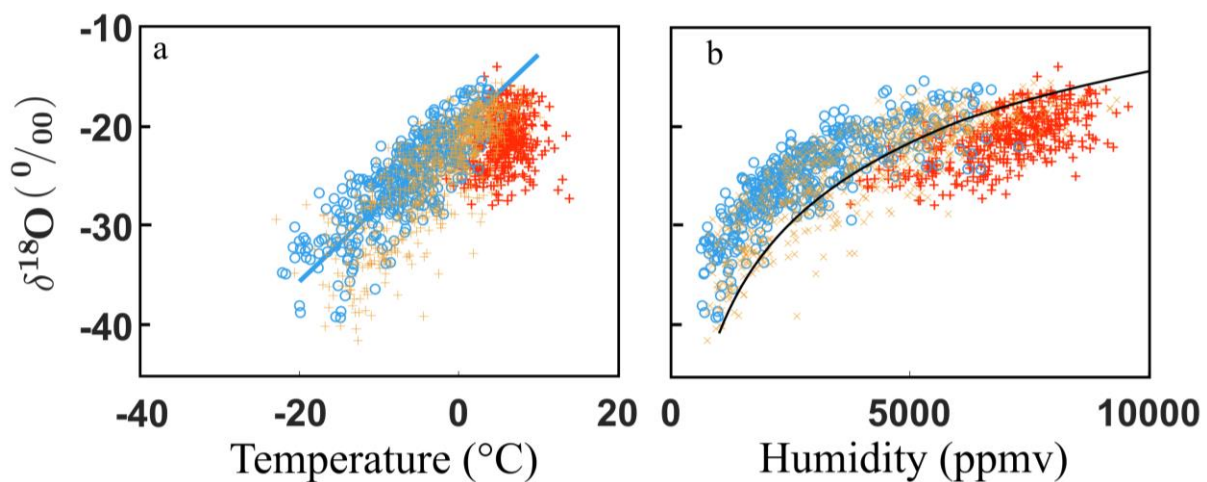
264 *Figure 2. From top to bottom: temperature, humidity, $\delta^{18}\text{O}$, δD and d-excess of atmospheric*
 265 *water vapor at 10 m. The full data series (black) was corrected following the calibration*
 266 *procedure described in Supporting Information Text S5, S6 and S7 and show clear seasonal*
 267 *variations. The grey period corresponds to the switch of instrument (from L1102-i to L2130-i).*
 268 *Note that different correction factors were implemented for the first instrument and the second*
 269 *one.*

270

271 Our dataset depicts a clear co-variance in temperature, humidity, and water vapor $\delta^{18}\text{O}$. On the
 272 contrary, we observe a global anti-correlation between d-excess and $\delta^{18}\text{O}$ ($R=-0.68$) or δD . The
 273 $\delta^{18}\text{O}$ vs temperature slope over the full record (Figure 3a) is $0.62 \text{‰} \cdot \text{°C}^{-1}$ for the entire series

274 (0.78 ‰.°C⁻¹ when considering only winter, i.e. DJF). This relationship between water vapor
 275 $\delta^{18}\text{O}$ and temperature lies within previous estimates in the region. The temporal slope observed
 276 at the coastal Greenland site of Ivittuut is smaller (0.37 ‰.°C⁻¹, Bonne et al., 2014) and such
 277 a low value could be linked to the latitude of Ivittuut, lower than at Ny-Ålesund. Over the
 278 northwest Greenland ice sheet, the isotopic record of the NEEM station spans summer only,
 279 and is marked by strong diurnal cycles probably associated with local exchanges between snow
 280 surface and water vapor superimposed on the synoptic signal (Steen-Larsen et al., 2013). The
 281 NEEM dataset spanning 3 consecutive summer seasons is associated with a temporal slope of
 282 1.1 ‰.°C⁻¹, i.e. almost twice larger than the $\delta^{18}\text{O}$ vs temperature slope of our record.

283 The observed relationship between humidity and water vapor $\delta^{18}\text{O}$ is displayed in Figure 3b.
 284 The general pattern is very close to the theoretical relationship between water vapor $\delta^{18}\text{O}$ and
 285 humidity predicted by a Rayleigh distillation along a trajectory starting from evaporation over
 286 the mid-latitude ocean (see black line in Figure 3b). The relatively low water vapor $\delta^{18}\text{O}$ values
 287 (-40 to -15 ‰) indicate that the recharge of water vapor by local ocean evaporation is small at
 288 least during winter. Indeed, the isotopic composition of water vapor evaporating over the open
 289 ocean in North Atlantic is about -8 to -20‰ (Benetti et al., 2017, 2018; Bonne et al., 2019;
 290 Steen-Larsen et al., 2015, 2017) so that a strong recharge would lead to higher $\delta^{18}\text{O}$ values than
 291 observed in winter. In summer, the relatively high values of $\delta^{18}\text{O}$ values of water vapor can be
 292 due to some local evaporation. The results obtained here suggest that the variability of the $\delta^{18}\text{O}$
 293 signal in winter is driven by different degrees of distillation of advected air masses (Dansgaard,
 294 1964; Rayleigh, 1902) in addition to a switch of distant moisture sources (Vázquez et al., 2016).



295

296 *Figure 3. Observed relationship between surface water vapor $\delta^{18}\text{O}$ and surface air temperature*
 297 *(a) and between surface water vapor $\delta^{18}\text{O}$ and humidity (b). The colors of data points vary*

298 *according to the seasons: blue circles for winter (DJF), yellow crosses for autumn (SON) and*
299 *spring (MAM), red crosses for summer (JJA) seasons. The blue line in Figure 3a is the linear*
300 *fit between $\delta^{18}\text{O}$ and temperature during winter (DJF), the black line in Figure 3b is the model*
301 *output from MCIM (Mixed Cloud Isotopic Model, Ciais & Jouzel, 1994, initial conditions:*
302 *surface pressure = 1015 hPa, surface temperature = 290K and surface relative humidity =*
303 *80%).*

304 **3.2. Seasonal and diurnal variabilities**

305 Seasonal variations are observed unequivocally in both temperature and humidity (Table 1)
306 which reach maximum values in summer, respectively 5.0°C and 6900 ppm, and minimum
307 values in winter, respectively -7.0°C and 2800 ppm (average values over JJA and DJF
308 respectively over the whole time period). Similarly, higher values are observed in summer for
309 water vapor isotopic composition (+4.1 ‰ and +25.5 ‰ in average for $\delta^{18}\text{O}$ and δD respectively
310 compared to winter values), as expected from the temperature-to-isotopic composition
311 relationship. The d-excess signal depicts lower values in summer than in winter, hence in anti-
312 correlation with $\delta^{18}\text{O}$. This result is similar to observations by Bonne et al. (2014) in South
313 Greenland but opposite to the d-excess maximum observed in summer precipitation in central
314 Greenland (Kopec et al., 2019).

315 The intra-seasonal variability is much larger in winter than in summer: the winter standard
316 deviation is almost twice larger for temperature, $\delta^{18}\text{O}$ and δD compared to summer. The
317 humidity and d-excess variability is also larger in winter than in summer. The strong winter
318 variability motivates us to explore the associated mechanisms and their potential links to
319 synoptic scale events.

320

Year	Summer (JJA)						Winter (DJF)						Full year (Jan to Dec)					
	Hum (ppmv)	RH (%)	T (°C)	$\delta^{18}\text{O}$ (‰)	δD (‰)	d-xs (‰)	Hum (ppmv)	RH (%)	T (°C)	$\delta^{18}\text{O}$ (‰)	δD (‰)	d-xs (‰)	Hum (ppmv)	RH (%)	T (°C)	$\delta^{18}\text{O}$ (‰)	δD (‰)	d-xs (‰)
14	6800 ± 1200	82 ± 9	3.9 ± 2.3	-20.9 ± 3.2	-158.7 ± 21.9	8.4 ± 5.4	2400 ± 1400	65 ± 12	-9.1 ± 6.3	-27.2 ± 6.2	-199.6 ± 46.3	17.6 ± 7.3	//	//	//	//	//	//
15	6900 ± 1200	76 ± 11	5.7 ± 2.4	-22.1 ± 3.2	-166.0 ± 22.7	10.6 ± 3.6	3000 ± 1400	69 ± 11	-5.7 ± 4.9	-25.0 ± 4.3	-183.9 ± 32.2	16.5 ± 6.9	4200 ± 2200	72 ± 12	-2.1 ± 7.1	-24.0 ± 5.0	-177.2 ± 36.0	14.9 ± 7.5
16	7000 ± 1300	77 ± 11	5.4 ± 2.4	-21.1 ± 3.0	-160.8 ± 16	8.3 ± 5.4	2700 ± 1700	67 ± 14	-8.2 ± 6.2	-25.0 ± 4.9	-180.7 ± 35.4	19.3 ± 7.9	4900 ± 2200	73.5 ± 12	-0.8 ± 6.1	-22.5 ± 4.3	-168.1 ± 30	12.2 ± 7.4
17	6900 ± 1100	79 ± 9	4.7 ± 2	-21.0 ± 3.1	-157.0 ± 21.3	11.0 \pm 4	3100 ± 1300	66 ± 12	-4.9 ± 4.1	-24.0 ± 4.0	-177.8 ± 30.9	14.5 ± 5.9	4200 ± 2400	70 ± 12	-2.7 ± 7.3	-24.5 ± 5.5	-180.1 ± 38.9	15.9 ± 7.5
18	7000 ± 1300	78 ± 9	5.1 ± 2.1	-20.7 ± 3.1	-156.9 ± 21.7	8.9 ± 4.4	//	//	//	//	//	//	//	//	//	//	//	//
TOT	6900 ± 1200	79 ± 10	5.0 ± 2.3	-21.2 ± 3.1	-159.9 ± 21.2	9.5 ± 4.7	2800 ± 1500	68 ± 12	-7.0 ± 5.7	-25.3 ± 5.1	-185.4 ± 37.6	17.0 ± 7.3	4600 ± 2300	72 ± 12	-1.6 ± 6.7	-23.6 ± 5.1	-175.0 ± 36.1	14.0 ± 7.4

322 *Table 1. mean and standard deviation of meteorological parameters and isotopic composition*
323 *calculated from hourly means. Total standard deviation is calculated from the concatenated*
324 *seasons at hourly resolution. Summer 14 corresponds to JJA of year 2014 and winter 14*
325 *corresponds to December 2014, January 2015 and February 2015.*

326 In contrast with results of water vapor time series from sites marked by large diurnal variations
327 in local boundary layer winds or evapotranspiration (Berkelhammer et al., 2016; Bréant et al.,
328 2019; Kopec et al., 2014; Steen-Larsen et al., 2013), diurnal variations are very small in our
329 record, with diurnal amplitudes of temperature, humidity or $\delta^{18}\text{O}$ variations below 2°C, 870
330 ppm and 3.2 ‰ respectively, independently of the season. In our dataset, the mean diurnal
331 variations have values comparable to the lowest diurnal variability observed in polar sites
332 marked by large boundary layer variations (Bréant et al., 2019). This implies that our record is
333 moderately influenced by diurnal changes in local surface fluxes and boundary layer mixing.
334 This supports the finding that the Svalbard surface water vapor isotopic composition does not
335 bear a clear signature of exchange with the local oceanic surface on diurnal time scales.

336 **3.3. Comparison between sea level AWIPEV and 474 m a.s.l. Zeppelin observatory** 337 **isotopic vapor data**

338 During 2 weeks, in May 2015, water vapor isotopic composition was measured at two sites in
339 parallel (Figure S4). A very high correlation is observed between the two data sets ($R > 0.9$ for
340 humidity and $\delta^{18}\text{O}$, $R = 0.8$ for d-excess), with only a slight offset for humidity (average mixing
341 ratio of 4000 ppmv and 3900 ppmv for AWIPEV station and Mount Zeppelin respectively),
342 and for the mean $\delta^{18}\text{O}$ (-24.0 ‰ and -23.3 ‰ for AWIPEV station and Mount Zeppelin
343 respectively). Temperatures at both sites are well correlated ($R = 0.87$) during this period, but

344 show an average difference of -3°C between Mount Zeppelin and AWIPEV. The high
345 correlation between the two temperature records agrees with the high co-variance between both
346 isotopic signals but cannot explain why the offset between the two $\delta^{18}\text{O}$ series is smaller than
347 expected from the temperature vs $\delta^{18}\text{O}$ slope determined in section 3.1. A better explanation for
348 this small shift is probably to be found in calibration issues with the Mount Zeppelin instrument
349 (Figure S7). In the following discussion, we mainly focus on the water isotopic variability, and
350 our findings are not challenged by this offset.

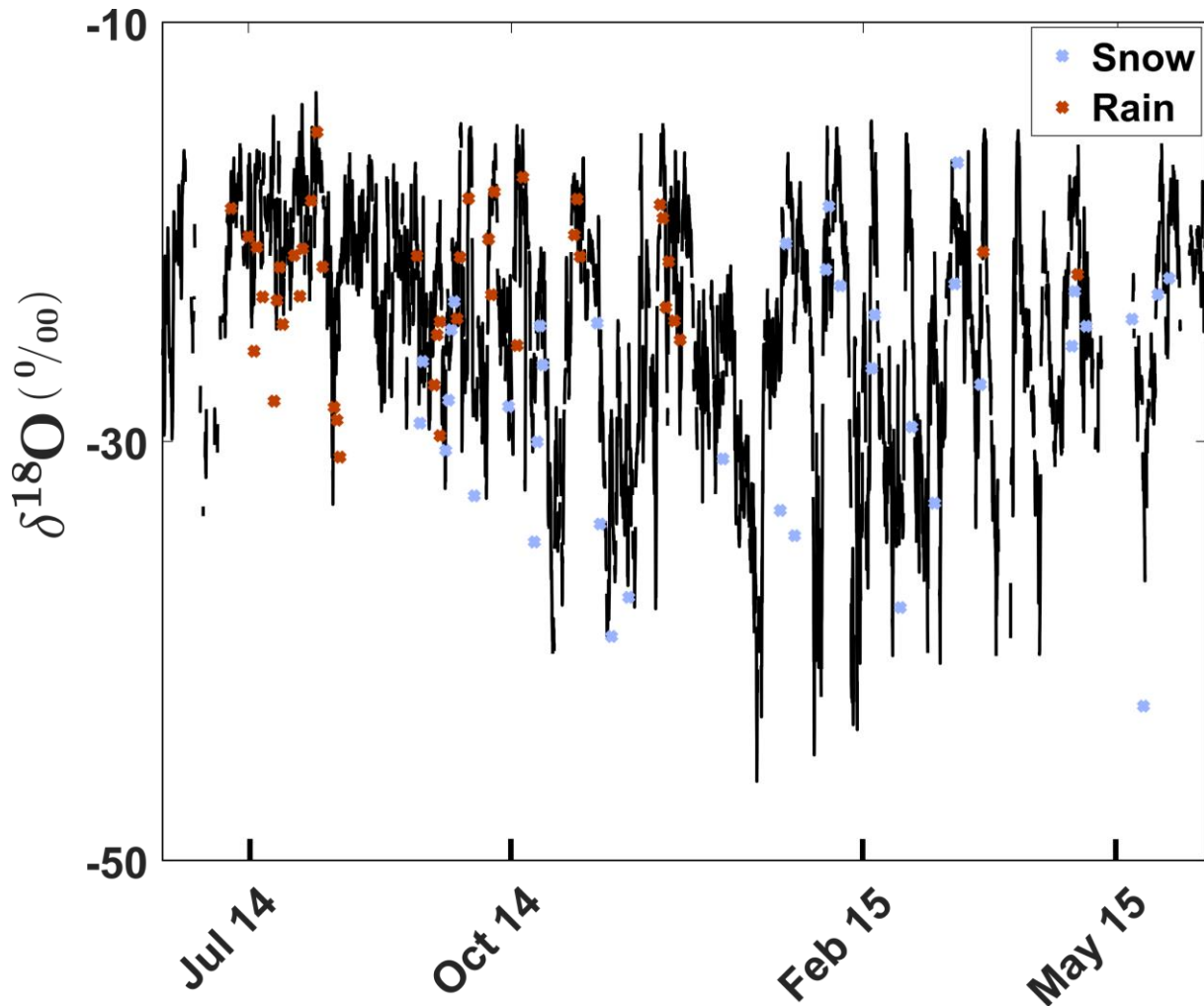
351 The strong correlation between the vapor isotopic composition measurement datasets near the
352 surface and at 474 m a.s.l. justifies the assumption that the variations of the water vapor isotopic
353 signal at Ny-Ålesund reflect the dynamics of the lower troposphere moisture isotopic
354 composition driven by large scale regional variability, and not local boundary layer dynamics
355 or sources. This finding is also supported by the analysis of almost 20 years of radiosondes
356 measurements in Svalbard (Maturilli & Kayser, 2017), showing that local boundary layer
357 characteristics are directly influenced by large scale dynamics such as Arctic Oscillation
358 changes, even in winter time when an inner fjord weather regime can superimpose.

359 **3.4. Comparison between vapor and precipitation isotopic composition**

360 The full data series of the isotopic composition of precipitation together with surface air
361 temperature measurements during precipitation days is presented in supporting information
362 (Text S10 and Figure S11). The average $\delta^{18}\text{O}$ and d-excess over the measurement period are -
363 9.6 ± 4.6 ‰ and 6.2 ± 10.5 ‰ with significant seasonal variations. The variability is twice
364 larger during winter than during summer for $\delta^{18}\text{O}$, as already observed for the vapor isotopic
365 composition (Table 1). This is mainly due to the large range of temperature variations in winter
366 compared to summer (factor of 2 between both variabilities).

367 The precipitation $\delta^{18}\text{O}$ values observed at Ny-Ålesund are coherent with the precipitation $\delta^{18}\text{O}$
368 values in the Arctic region as documented by the IAEA/WMO Global Network for Isotopes in
369 Precipitation (GNIP) database with monthly $\delta^{18}\text{O}$ values varying between -9 and -17 ‰ in
370 North Sweden. In Ivittuut (Greenland), Bonne et al. (2014) also found similar $\delta^{18}\text{O}$ values for
371 precipitation between -5 and -20 ‰. Svalbard Ice core $\delta^{18}\text{O}$ variations from (Isaksson et al.,
372 2005) show a range of more depleted $\delta^{18}\text{O}$ values (around -16 to -17‰), which are consistent
373 with a stronger distillation towards higher altitudes (drilling altitude of ice cores of 1250 and
374 750 m, respectively) than for a coastal site such as Ny-Ålesund (Smith & Evans, 2007; Stern &
375 Blisniuk, 2002).

376 In order to compare the precipitation isotopic signal to the vapor signal, we calculated the
377 theoretical isotopic composition of a vapor at equilibrium with each precipitation sample.
378 Equilibrium fractionation coefficients are temperature-dependent and it is not obvious to define
379 which equilibrium temperature should be used within the atmospheric column between the
380 cloud base (where precipitation forms) and surface temperature (where liquid precipitation can
381 be reequilibrated with the surrounding water vapor measured by the Picarro instrument).
382 Several sensitivity tests were performed (Text S10 and Figure S12) and equilibrium
383 fractionation coefficients were finally computed with 2-meter air temperature for rain samples
384 (because of possible exchange with water vapor at this sampling height), and with cloud base
385 height temperature for solid precipitation. Indeed, we assumed that the isotopic composition of
386 snow does not significantly change during its descent and possible partial sublimation along the
387 atmospheric column (Maturilli & Kayser, 2017). For our calculation, we used liquid-vapor and
388 solid-vapor fractionation coefficients at equilibrium from Majoube (1971) and Merlivat and
389 Nief (1967).



390

391 *Figure 4. Comparison over one-year (from 01/06/2014 to 01/06/2015) of the $\delta^{18}\text{O}$ measured in*
392 *the vapor (black line, hourly averaged) and the theoretical computed $\delta^{18}\text{O}$ of vapor in*
393 *equilibrium with precipitation samples collected daily at AWIPEV station (light blue for snow*
394 *and red for rain).*

395 Figure 4 and Figure S13 show the reconstructed water vapor $\delta^{18}\text{O}$ series calculated from
396 precipitations (see also Figure S12 and S13) along with the $\delta^{18}\text{O}$ directly measured in the vapor.
397 Both $\delta^{18}\text{O}$ series share around 60% of variance ($R=0.78$). Such a good correlation shows that
398 synoptic events affecting the water vapor isotopic composition should also be recorded in the
399 snow and rain when these synoptic events are associated with precipitation. The remaining
400 unexplained variance can be due to kinetic effects occurring 1) during precipitation re-
401 evaporation within the atmospheric column or most probably during the 24 hours' period
402 between precipitation and sampling, 2) during precipitation formation in supersaturation
403 condition or mixed-phase clouds.

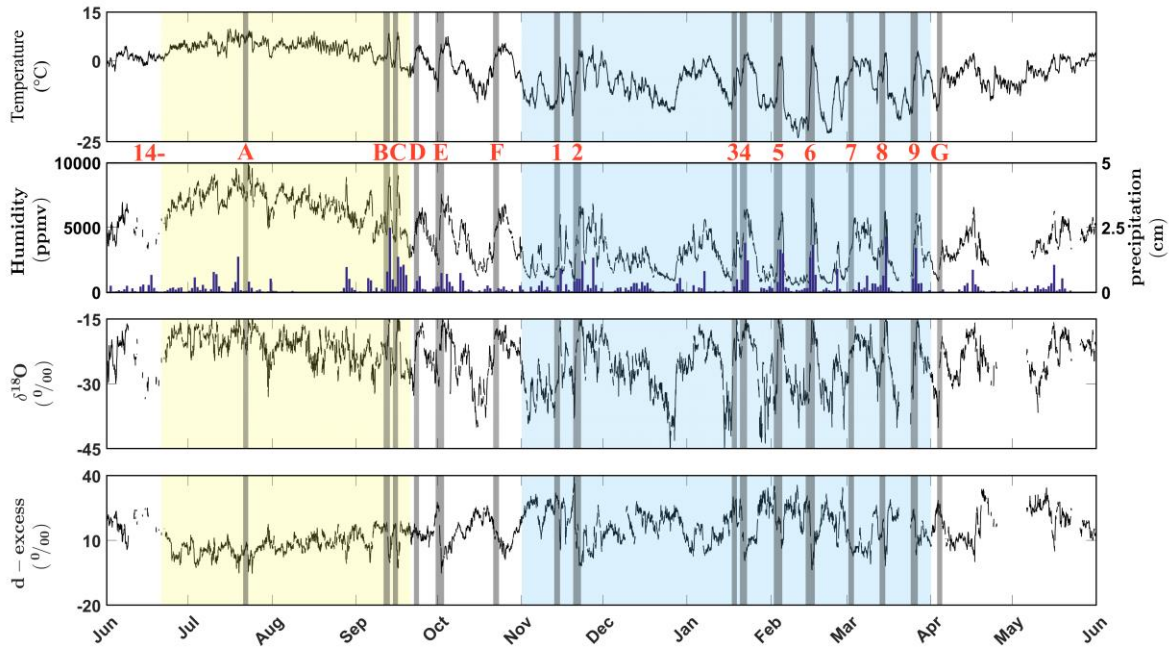
404 **4. Investigation of winter synoptic events and perspectives**

405 From the absence of a significant diurnal cycle, the coherency between day-to-day variations
406 recorded in vapor and precipitation isotopic measurements, as well as the similarity between
407 data from stations at two different altitudes, we have demonstrated that the signal recorded at
408 AWIPEV is dominated by day-to-day variability associated with synoptic weather. We can
409 hence use surface vapor measurements to study large scale processes in this sector and we
410 concentrate in the following on the important winter variability of temperature, humidity and
411 water stable isotopes. Moreover, Rinke et al. (2017) and Zhang et al. (2004) have shown that
412 the cyclone intensity and frequency are higher in winter which makes this season of particular
413 interest for the Svalbard region.

414 **4.1. Detection of synoptic events**

415 We first characterize the signature of synoptic events on the vapor isotopic composition from
416 our time series. Synoptic events are defined as events of a time scale of 1 to 5 days and a spatial
417 scale of several hundred to several thousand kilometers. In the Arctic, increases of the humidity
418 of 3000 ppmv within a period of two days, following the criteria used by Bonne et al., (2014),
419 are associated with synoptic events, particularly in winter when almost all events are linked to
420 anomalies in temperature due to air masses coming from the North Atlantic (Nomokonova et
421 al., 2020). We use these criteria to identify the humidity peaks from our time series in Svalbard
422 and pinpoint synoptic events. During the period from 01/06/2014 to 01/06/2015 (Figure 5),

423 these large and abrupt events provide 39% of the total precipitation amount (as identified using
 424 ERA5 total precipitation variable) and are associated with large peaks in the water vapor
 425 isotopic composition, i.e. a systematic increase in $\delta^{18}\text{O}$ and in most cases a decrease in d-excess.



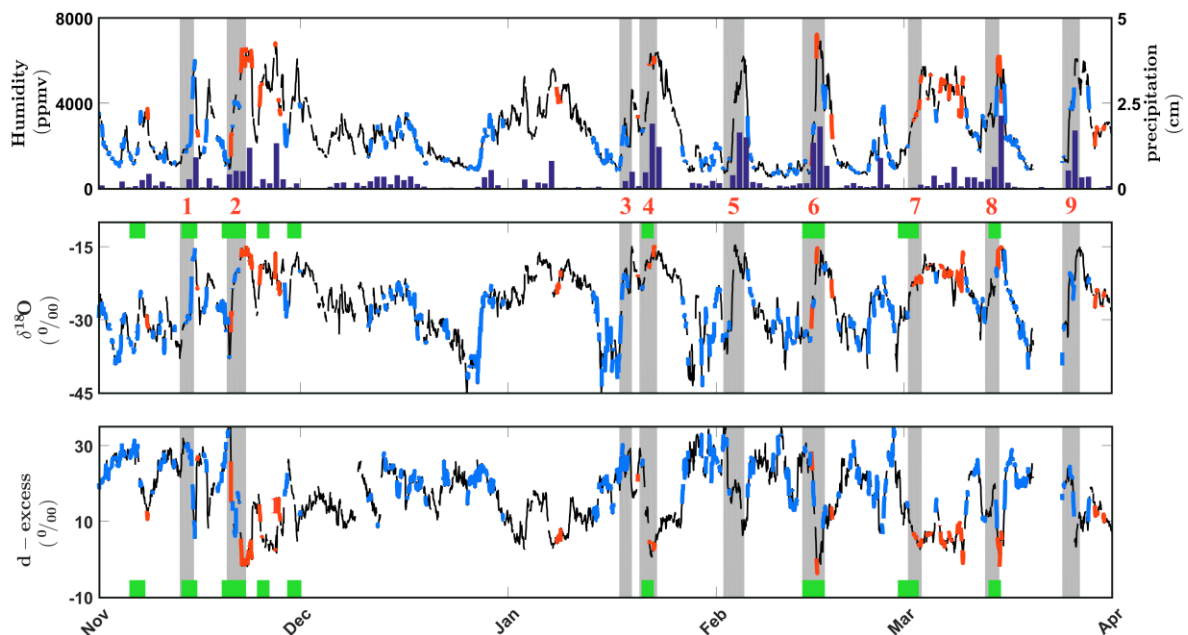
426

427 *Figure 5. One-year data series (01/06/2014 to 01/06/2015) of measurements at AWIPEV*
 428 *station. Blue bars in the second panel stand for daily precipitation amount derived from ERA-*
 429 *5. In yellow: summer season, in blue: extended winter season (from November to March). Grey*
 430 *bars are humidity peaks defined as an increase of 3000 ppmv (or more) within 2 days*
 431 *(numbered from 14-1 to 14-9 during extended winter, and from 14-A to 14-G out of this period).*

432 Over the full year period, we identify 16 such synoptic events numbered 14-1 to 14-9 and 14-
 433 A to 14-G: only 3 are detected during the warm plateau in summer (14-A, 14-B and 14-C in
 434 Figure 5), 2 of them occurring at the very end of the summer period when temperature and
 435 humidity start to decrease (14-B and 14-C). The other 13 occur outside of this period. Winter
 436 climate variability is dominated by the moist events occurring 5 to 9 times between the months
 437 of November and March, which is consistent with the relatively high increase of vertically
 438 integrated water vapor content in the region in winter (Nomokonova et al., 2020; Rinke et al.,
 439 2019). In the following, we thus focus this study on the humidity peaks over the coldest period
 440 (i.e. temperature below 5°C, large predominance of snow precipitation) from 1st November to
 441 31st March, hence events 14-1 to 14-9 in Figure 5 and Figure 6. Moreover, such events are
 442 expected to be an important signal in the accumulated snow in the region which has a direct
 443 application for the interpretation of ice cores (Divine et al., 2008; Isaksson et al., 2005; Opel et

444 al., 2009). These nine events, each one associated with a temperature increase larger than 7°C ,
 445 systematically display an increase in $\delta^{18}\text{O}$ larger than 7‰ within 2 days. The d-excess generally
 446 shows a decreasing signal larger than 10‰ within 2 days (observed for all events except for
 447 14-3).

448 The same detection routine (increase of more than 3000 ppmv in 2 days) is then applied over
 449 the four winters (November to March) of our record, for years 2014 to 2018. In total, we detect
 450 28 events (Figure 6 for winter 14, Figure S14 for following years). All of these humidity events
 451 display a significant increase of $\delta^{18}\text{O}$ (more than 7‰ in 2 days). A majority of these peaks
 452 seem associated with a decrease of d-excess.



453

454 *Figure 6. Links between the water vapor isotopic composition and air mass origin over winter*
 455 *14. Grey bars are humidity peaks as defined in the text. Red and blue lines correspond to air*
 456 *masses with specific source location (North Atlantic and Arctic respectively) estimated with*
 457 *Hysplit (see text). Time periods with particularly high anti-correlation ($R < -0.7$) between $\delta^{18}\text{O}$*
 458 *and d-excess are highlighted by the green bars.*

459 **4.2. Possible mechanisms at play**

460 As mentioned in the introduction, d-excess variations can be used to trace changes in moisture
 461 sources. We investigate here how the combination of surface vapor $\delta^{18}\text{O}$ and d-excess can
 462 provide information on the origin of the air mass trajectories coming to Svalbard during our
 463 winter humidity peaks. For this purpose, we calculate the correlation coefficient between the

464 increase of $\delta^{18}\text{O}$ and the corresponding hourly variation of d-excess over the 2 consecutive days
465 of one identified humidity peak. We tag in green in Figure 6 and Figure S14 the time periods
466 with both (i) a significant increase in $\delta^{18}\text{O}$ ($>7\text{‰}$) and (ii) a significant anti-correlation between
467 d-excess and $\delta^{18}\text{O}$ ($R < -0.7$).

468 Several explanations can be proposed for the observed anti-correlation between d-excess and
469 $\delta^{18}\text{O}$ over the highlighted green periods. A first effect can be linked to the role of precipitation
470 and transport. A $\delta^{18}\text{O}$ vs d-excess anti-correlation can be obtained in the case of intense
471 distillation as observed in the water vapor isotopic composition in continental polar regions
472 after a long trajectory without significant recycling or high in the atmosphere (Risi et al., 2010;
473 Touzeau et al., 2016). This effect could play a role in the polar Svalbard context and can best
474 be evidenced using a logarithm definition of the d-excess (Dütsch et al., 2017; Uemura et al.,
475 2012), see details in Text S2 and Figure S2. Still, the observed range of $\delta^{18}\text{O}$ values is rather
476 high, ruling out a case of intense distillation. The other dominant effects are linked to
477 evaporation and re-evaporation which occur along the water mass trajectory. Because of kinetic
478 effects, evaporation of water under relatively dry air conditions should lead to lower $\delta^{18}\text{O}$ and
479 higher d-excess in vapor, based on the simple approach of Merlivat and Jouzel (1979) applied
480 to several systems (e.g. Sodemann et al., 2017); this effect probably plays a role here. Then, as
481 shown in Risi et al. (2008), re-evaporation is one of the major processes explaining the isotopic
482 signal in regions with strong local precipitation, characterized by the so-called amount effect
483 (decrease in $\delta^{18}\text{O}$ and increase in d-excess for strong precipitation rate). Rain re-evaporation
484 leads to an increase of d-excess in the water vapor. However, this effect is dominant mostly in
485 tropical regions or below clouds in case of dry air advection from the free troposphere. We are
486 studying here moist events with a large proportion of snow precipitation so that rain re-
487 evaporation is probably not the main driver of our isotopic signal. Finally, another possible
488 process is the sublimation of snow (Kopeck et al., 2019; Pang et al., 2018). However, sublimation
489 of snow is an effect that is only significant in the continental polar regions when moisture
490 travels above the continental ice sheet, which differs from our coastal Svalbard context.

491 We thus conclude that the process explaining the largest part of the d-excess vs $\delta^{18}\text{O}$
492 relationship in the water vapor over Svalbard is most likely linked with a change in evaporative
493 conditions in the moisture source region. In particular, low d-excess is generally associated with
494 high relative humidity at evaporation because kinetic fractionation is reduced when the air is
495 saturated with water vapor. Where relative humidity of the atmosphere is low, for instance near
496 the sea ice margins or during SLOE events (Strong Large-scale Ocean Evaporation), d-excess

497 values in surface vapor are high (Kurita, 2003). This mechanism has already been proposed to
 498 explain high d-excess values observed in the Arctic region (Aemisegger, 2018; Aemisegger &
 499 Sjolte, 2018; Bonne et al., 2019; Steen-Larsen et al., 2015) and should also be considered to
 500 understand our records. Because of the probable influence of source evaporative conditions and
 501 distillation along the trajectory on the isotopic signal, we thus focus in the following on the role
 502 of changes in air mass trajectories and origin of air masses using back-trajectories calculated for
 503 each wet winter (humidity peak) event.

504
 505
 506

507 4.3. Back-trajectories and isotopic signature

508 The Hysplit back-trajectories were first clustered according to their origin: the back-trajectories
 509 with their origin (first 2 days) within the Arctic sector (latitude higher than 80°N and longitude
 510 between 60°W and 60°E) are displayed in blue; the back-trajectories with their origin within
 511 the Atlantic sector (latitudes below Iceland) are displayed in red (Figures 6, 7 and S14).

Year	14									15							16							17					Tot
Humidity peaks number	1	2	3	4	5	6	7	8	9	1	2	3	4	5	6	7	1	2	3	4	5	6	7	1	2	3	4	5	28
Atlantic source		X		X		X	X	X		X		X	X		X	X		X			X	X	X		X	X	X	X	18
Other source	X		X		X				X		X			X			X		X	X				X					10
($\delta^{18}\text{O}$,d-excess): R<-0.7	X	X		X		X	X	X		X	X	X	X		X						X	X				X			14
($\delta^{18}\text{O}$,d-excess): R>-0.7			X		X				X					X	X	X	X	X	X		X		X	X		X	X	14	

512

513 *Table 2. Classification of extended winter humidity peaks (Figure 6 and Figure S14). “Atlantic*
 514 *source” means that humidity peaks are associated with North Atlantic air masses while “other*
 515 *source” mainly stands for Arctic origins. The last two lines separate events associated with a*
 516 *specific isotopic signature (high anti-correlation between $\delta^{18}\text{O}$ and d-excess: $R < -0.7$) from*
 517 *others (no high anti-correlation between $\delta^{18}\text{O}$ and d-excess or positive correlation). Red boxes:*
 518 *moist events associated with North Atlantic origins based on the Hysplit diagnostic. Blue boxes:*
 519 *moist events mainly associated with Arctic origins based on the Hysplit diagnostic. The specific*
 520 *isotopic signature (fifth line) is most of the times associated with North Atlantic origins (red*
 521 *boxes). On the fifth line (sixth line), blue boxes (red boxes) contradict the general*
 522 *interpretation. Grey boxes: events for which back-trajectories are shown in Figure 7.*

523 When comparing the anti-correlation between $\delta^{18}\text{O}$ and d-excess with the air mass origin over
 524 Svalbard, we observe that in most of the cases, the synoptic events with strong $\delta^{18}\text{O}$ vs d-excess

525 anti-correlation (14 events) are associated with an air mass origin located in the north Atlantic
526 during the humidity peak (Table 2, 12 peaks over 14). For all these 14 events, air masses have
527 an Arctic origin prior to the humidity increase. On the other hand, out of the 14 events with no
528 clear anti-correlation detected, 8 are related to different air mass source (Table 2) mainly from
529 the Arctic sector (Greenland, Siberia or Scandinavia). However, for 6 events (bold in the last
530 column of Table 2), there is no clear anti-correlation between $\delta^{18}\text{O}$ and d-excess although air
531 originates from the North Atlantic. We now illustrate in Figure 7 these different behaviors by
532 focusing on 4 particular humidity peaks (16-5, 15-2, 17-1, 16-2) and complementing then by
533 the Flexpart diagnostic (Text S9, Figures S15)

534 The humidity peak 16-5 (Figure 7, first panel) has a water isotopic signal showing a clear anti-
535 correlation between the abrupt increase in $\delta^{18}\text{O}$ (more than 9 ‰) and the abrupt decrease in d-
536 excess (more than 10 ‰) over 2 consecutive days (1-3 February). In parallel, back-trajectories
537 shift rapidly (in less than one day) from a situation with air of Arctic origin to a situation with
538 air of Atlantic origin. This example illustrates the general behavior observed for events marked
539 in red on the fifth line in Table 2: an anti-correlation between the increase of $\delta^{18}\text{O}$ and the
540 decrease of d-excess over winter humidity peak is the signature of a rapid shift of air origin
541 from Arctic origin to oceanic mid-latitude (Atlantic region). Flexpart footprints help us to refine
542 the location of the air parcel origin and allow us to relate this characteristic isotopic signature
543 to a shift to a source located in the North Atlantic Ocean at a latitude below 60°N (Figure S15).

544 For only two events out of the 14 events identified over the winters of our study (14-1 and 15-
545 2), the anti-correlation between an increase in $\delta^{18}\text{O}$ and a decrease in d-excess is not associated
546 with a shift of moisture origin toward the Atlantic Ocean (Table 2). During the event 15-2
547 (second panel of Figure 7), air origin shifts from the Arctic ocean covered by sea ice to open
548 waters of Barents and Greenland seas. We propose that this strong change of air mass origin
549 can lead to the observed isotopic signal. This shift in air mass origin is confirmed by additional
550 footprints analyses performed using the Flexpart tool: a large fraction of Flexpart back-
551 trajectories show an origin of air mass in the atmospheric boundary layer above Arctic sea-ice
552 before the humidity peak to a local source, suggesting that the moisture increase results from
553 local evaporation (Figure S15).

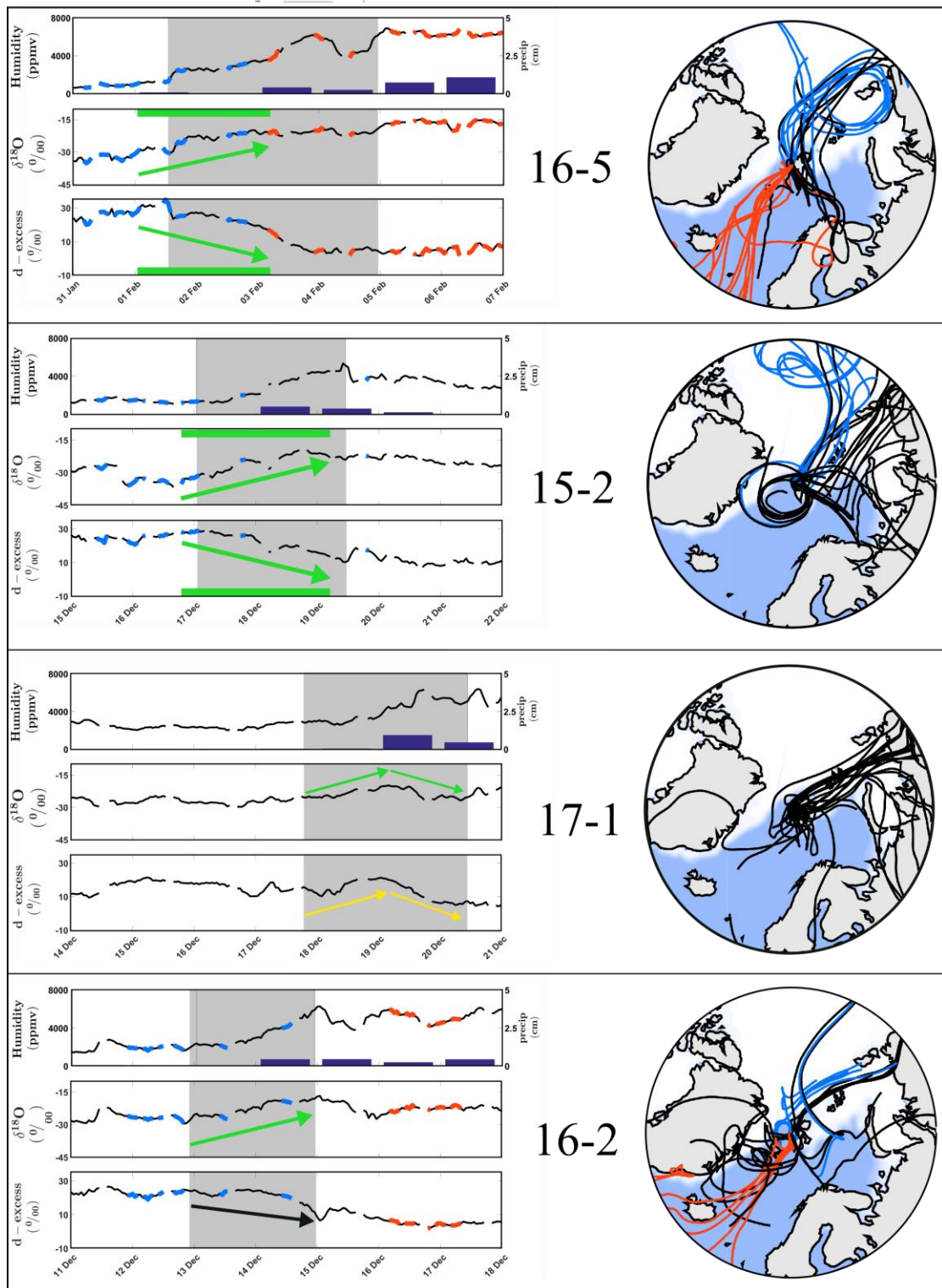
554 14 events do not show any strong anti-correlation between $\delta^{18}\text{O}$ and d-excess (Table 2, last
555 column). In a majority of cases (8 peaks over 14), the shift of air mass trajectories happens
556 within the Northern sector (Arctic: Greenland, Siberia or Scandinavia). This is the case of the
557 humidity peak beginning on 16 December 2017 (event 17-1, third panel of Figure 7): the $\delta^{18}\text{O}$

558 increase (more than 12 ‰) and the following decrease (slightly less than to 8 ‰), are not anti-
559 correlated with the d-excess signal. In fact, the d-excess is correlated with $\delta^{18}\text{O}$ ($R > 0.7$) during
560 the abrupt increase in humidity. In parallel, the back-trajectories display a change in the origin
561 of air parcels within the Northern sector: from continental region of Siberia (14-18 December)
562 to sea ice margin close to Svalbard (18-20 December). At the beginning of the event, relatively
563 low d-excess could be explained by soil evaporation in the Siberian continental regions
564 (Aemisegger et al., 2014). At the humidity maximum, the d-excess decrease can be explained
565 by local oceanic evaporation in a moist atmosphere, hence under a small air-sea humidity
566 gradient. The pattern of change in air mass origin is confirmed by the Flexpart footprints
567 analysis (Figure S15, third panel).

568 For the other events (15-6, 16-2, 16-6, 17-2, 17-4 and 17-5) during which the change of air mass
569 origin (from Arctic to North Atlantic origin) is not associated with d-excess vs $\delta^{18}\text{O}$
570 anticorrelation signature, the shift of air mass origin is either too slow or does not involve
571 latitudes southern than 65°N to be imprinted in the water isotopes records as illustrated for event
572 16-2 in Figure 7 (fourth panel). This conclusion is strengthened by Flexpart footprints which
573 show that the red back-trajectories computed with Hysplit can be misleading: at the humidity
574 maximum, most of the air masses originate in fact locally, from areas located at amplitudes
575 higher than 70°N of the Greenland Sea (Figure S15, fourth panel). This explains why the
576 isotopic signal is ambiguous over this particular event.

577

578



579

580 *Figure 7. Examples of 4 humidity peaks (16-5, 15-2, 17-1, 16-2). The left panels display the*
 581 *humidity, precipitation, $\delta^{18}\text{O}$ and d-excess records over 7 days including the humidity peak*
 582 *event (in grey). The right panels display the associated 5 days back-trajectories computed with*
 583 *Hysplit. On both panels, red lines are for air parcel originating from the North Atlantic sector*
 584 *(first 2 days over the 5 days of calculation), while blue lines stand for the Arctic sector. Black*

585 *lines and black back-trajectories are unlabeled. Arrows indicate the correlation between $\delta^{18}\text{O}$*
586 *and d-excess: pairs of green arrows are for high anti-correlation, pairs of green and yellow*
587 *arrows are for high correlation and a pair of green and black arrow stands for no specific*
588 *correlation. Sea ice concentration is represented in white (calculated from ERA-5 reanalyses).*
589

590 **4.4. Implications**

591 Our exceptionally long water vapor isotopic dataset complements previous findings from
592 records of isotopic composition of water vapor in the North Atlantic and Arctic regions. In
593 particular, Bonne et al. (2015) also identified synoptic events during autumn, winter and spring
594 associated with the same kind of humidity peaks (more than 3000 ppmv increase in 2 days) in
595 Greenland at the Ivittuut station. In their study, all identified humidity peaks display a strong
596 anti-correlation between a $\delta^{18}\text{O}$ increase and a d-excess decrease and all events correspond to
597 an arrival of moisture from the Atlantic Ocean, south of Greenland. Such a pattern agrees with
598 our finding over the Svalbard region, i.e. the anti-correlation between $\delta^{18}\text{O}$ and d-excess
599 indicates a shift to Atlantic origin for the air masses during the cold season humidity peaks.
600 However, such an isotopic signature for an Atlantic moisture origin has more implications in
601 Svalbard since a significant proportion of air masses during humidity peaks does not come from
602 the Atlantic, opposite to South Greenland where humidity peaks systematically originate from
603 the Atlantic. Water isotopes bring thus a strong added value to identify shifts in Svalbard air
604 mass origins.

605 Our results have implication for the interpretation of d-excess in the Arctic region. While, high
606 d-excess values observed in the Arctic regions have been associated with moisture source in
607 high latitude regions covered by sea-ice (Kurita, 2003, Bonne et al., 2019; Steen-Larsen et al.,
608 2015), others suggest that a switch in moisture sources from low to high latitude should result
609 in a decrease of d-excess (Kopeck et al., 2019). Our study rather confirms the pattern where air
610 masses coming from high latitude carry vapor with higher d-excess: in fact, the humidity peaks
611 associated with air originating from the Arctic do not show any d-excess decrease, but rather
612 an increase as observed during events 14-9, 16-3, 17-1, 17-2, 17-5 with relatively high d-excess
613 values and positive correlation between $\delta^{18}\text{O}$ and d-excess.

614 First, the moist winter events are a significant source of precipitation over Svalbard. Our results
615 also have implications to be further explored in ice core science and climate modelling. From
616 the links made between vapor and precipitation measurements (section 3.4.), their isotopic

617 fingerprints archived in snow could help deciphering past changes in the origin of moisture
618 coming to the Arctic region using Svalbard ice core records.

619 Second, Svalbard is a key location to look at the atmospheric circulation and transport of moist
620 air at the boundary between north Atlantic and Arctic with a possible large influence of the sea
621 ice. Isotopic composition of water vapor brings an important diagnostic on shift of air mass
622 origin that should be combined with modelling approaches including water isotopes
623 description. One of the largest limitations when dealing with isotope-enabled models is their
624 inability to reproduce the large variations of d-excess in the north Atlantic and Arctic regions
625 (Risi et al., 2010; Steen-Larsen et al., 2017; Werner et al., 2011). Part of this limitation may be
626 linked to an inaccurate simulation of the water vapor isotopic composition in the boundary layer
627 or during sublimation over the sea ice or over snow (Bonne et al., 2019; Kopec et al., 2019;
628 Steen-Larsen et al., 2017; Werner et al., 2011). It may also be linked to an inaccurate
629 transportation model of the atmospheric moisture (e.g. isotopic composition of water vapor is
630 very sensitive to the model horizontal advection (Hendricks et al., 2000). Because Svalbard is
631 at a key location with alternation of moisture arrival from Arctic and Atlantic, the comparison
632 between our long water vapor isotopic record and atmospheric simulations may help
633 disentangling the influence of marine boundary layer processes and atmospheric circulation.

634 Finally, our study focused on the large humidity peaks occurring during winter but there is a
635 clear interest to look as well at the other circulation patterns during winter as well as other seasons
636 with a possible larger influence of Arctic air masses. While the isotopic pattern is not as
637 systematic as for the winter humidity peaks with North Atlantic origin, periods with moisture
638 originating from the Arctic may be characterized by an opposite isotopic signature. However,
639 Arctic air is often dry and calibration of water vapor isotopic record is still difficult at low
640 humidity (below 2000 ppmv) hence limiting such an application (Casado et al., 2016; Ritter et
641 al., 2016). A new generation of laser spectroscopy instrument and associated calibration set-up
642 should soon permit to address such limitations. Our full dataset is available (Zenodo repository)
643 and we encourage and welcome its use for other studies focusing on arctic air intrusions as well
644 as on more local processes, such as polar lows or local orographic effects of air flows in the
645 fjord.

646 **5. Conclusion**

647 We presented the first continuous multi-year record of water isotopes in surface water vapor at
648 Ny-Ålesund (Svalbard), a key location at the edge of the current Arctic sea ice winter extent.

649 We have evidenced that this dataset reflects the regional dynamics of the atmospheric water
650 cycle. In this region, winter weather regime is characterized by the recurrence of humid events
651 lasting a few days. Combining $\delta^{18}\text{O}$ and d-excess in the water vapor with back-trajectories, we
652 identify the isotopic signature of a shift of air mass origin from the Arctic to the North Atlantic
653 below 60°N through a positive peak of $\delta^{18}\text{O}$ anti-correlated with d-excess. The isotopic
654 signature of moisture transported from an Arctic source is less unequivocal but is generally
655 marked by positive peaks of both $\delta^{18}\text{O}$ and d-excess.

656 Here, we focused our analyses on winter wet events, but our record can also be used to further
657 explore the relationships between surface water vapor and precipitation isotopic composition
658 and changes in air mass origins or moisture evaporation conditions during other seasons and at
659 the inter-annual scale. This could be achieved using not only air mass back-trajectories as used
660 here but also more sophisticated diagnoses of moisture transport and evaporation conditions
661 (Papritz & Sodemann, 2018; Sodemann et al., 2008).

662

663

664 Acknowledgement:

665 This work was supported by the IPEV ARCTISO project, the ANR projects AC-AHC²,
666 GREENLAND, EAIIST and the LEFE program ADELISE. It was also funded by the
667 Fondation Prince Albert 2 de Monaco under the project Antarctic-Snow. We thank Nick
668 Hughes, from the Norwegian Meteorological Institute, for sharing sea ice observations, as
669 well as Ove Hermansen from the Norwegian Institute for Air Research on behalf of the
670 Norwegian Environment Agency. We acknowledge the staff from AWIPEV who took care of
671 the experiment for almost 5 years and collected precipitation every day. We also thank two
672 anonymous reviewers for their very useful comments regarding this paper.

673

674 Data Availability:

675 The full dataset archiving is underway and will be fully available through a Zenodo repository:
676 10.5281/zenodo.3689566. Until publication, the data set is with limited access.

677

678 References:

679 Aemisegger, F. (2018). On the link between the North Atlantic storm track and precipitation

680 deuterium excess in Reykjavik. *Atmospheric Science Letters*, 19(12), e865.

681 <https://doi.org/10.1002/asl.865>

- 682 Aemisegger, F., & Sjolte, J. (2018). A Climatology of Strong Large-Scale Ocean Evaporation Events.
683 Part II: Relevance for the Deuterium Excess Signature of the Evaporation Flux. *Journal of*
684 *Climate*, 31(18), 7313–7336. <https://doi.org/10.1175/JCLI-D-17-0592.1>
- 685 Aemisegger, F. (2018). On the link between the North Atlantic storm track and precipitation
686 deuterium excess in Reykjavik. *Atmospheric Science Letters*, 19(12), e865.
687 <https://doi.org/10.1002/asl.865>
- 688 Aemisegger, F., & Sjolte, J. (2018). A Climatology of Strong Large-Scale Ocean Evaporation Events.
689 Part II: Relevance for the Deuterium Excess Signature of the Evaporation Flux. *Journal of*
690 *Climate*, 31(18), 7313–7336. <https://doi.org/10.1175/JCLI-D-17-0592.1>
- 691 Aemisegger, F., Sturm, P., Graf, P., Sodemann, H., Pfahl, S., Knohl, A., & Wernli, H. (2012). Measuring
692 variations of $\delta^{18}\text{O}$ and $\delta^2\text{H}$ in atmospheric water vapour using two commercial
693 laser-based spectrometers: an instrument characterisation study. *Atmospheric Measurement*
694 *Techniques*, 5(7), 1491–1511. <https://doi.org/10.5194/amt-5-1491-2012>
- 695 Aemisegger, F., Pfahl, S., Sodemann, H., Lehner, I., Seneviratne, S. I., & Wernli, H. (2014). Deuterium
696 excess as a proxy for continental moisture recycling and plant transpiration. *Atmospheric*
697 *Chemistry and Physics*, 14(8), 4029–4054. <https://doi.org/10.5194/acp-14-4029-2014>
- 698 Alekseev, G., Kuzmina, S., Bobylev, L., Urazgildeeva, A., & Gnatiuk, N. (2019). Impact of atmospheric
699 heat and moisture transport on the Arctic warming. *International Journal of Climatology*,
700 39(8), 3582–3592. <https://doi.org/10.1002/joc.6040>
- 701 Angert, A., Cappa, C. D., & DePaolo, D. J. (2004). Kinetic ^{17}O effects in the hydrologic cycle: Indirect
702 evidence and implications. *Geochimica et Cosmochimica Acta*, 68(17), 3487–3495.
703 <https://doi.org/10.1016/j.gca.2004.02.010>
- 704 Arctic Monitoring and Assessment Programme. (2017). *Snow, Water, Ice and Permafrost in the Arctic*
705 *(SWIPA)*. Oslo, Norway:
- 706 Bailey, A., Noone, D., Berkelhammer, M., Steen-Larsen, H. C., & Sato, P. (2015). The stability and
707 calibration of water vapor isotope ratio measurements during long-term deployments.

- 708 *Atmospheric Measurement Techniques*, 8(10), 4521–4538. [https://doi.org/10.5194/amt-8-](https://doi.org/10.5194/amt-8-4521-2015)
709 4521-2015
- 710 Bastrikov, V., Steen-Larsen, H. C., Masson-Delmotte, V., Gribanov, K., Cattani, O., Jouzel, J., &
711 Zakharov, V. (2014). Continuous measurements of atmospheric water vapour isotopes in
712 western Siberia (Kourovka). *Atmospheric Measurement Techniques*, 7(6), 1763–1776.
713 <https://doi.org/10.5194/amt-7-1763-2014>
- 714 Benetti, M., Steen-Larsen, H. C., Reverdin, G., Sveinbjörnsdóttir, Á. E., Aloisi, G., Berkelhammer, M.
715 B., et al. (2017). Stable isotopes in the atmospheric marine boundary layer water vapour over
716 the Atlantic Ocean, 2012–2015. *Scientific Data*, 4(1), 160128.
717 <https://doi.org/10.1038/sdata.2016.128>
- 718 Benetti, M., Lacour, J. -L., Sveinbjörnsdóttir, A. E., Aloisi, G., Reverdin, G., Risi, C., et al. (2018). A
719 Framework to Study Mixing Processes in the Marine Boundary Layer Using Water Vapor
720 Isotope Measurements. *Geophysical Research Letters*, 45(5), 2524–2532.
721 <https://doi.org/10.1002/2018GL077167>
- 722 Berkelhammer, M., Noone, D. C., Steen-Larsen, H. C., Bailey, A., Cox, C. J., O’Neill, M. S., et al. (2016).
723 Surface-atmosphere decoupling limits accumulation at Summit, Greenland. *Science*
724 *Advances*, 2(4), e1501704. <https://doi.org/10.1126/sciadv.1501704>
- 725 Bintanja, R., & Selten, F. M. (2014). Future increases in Arctic precipitation linked to local evaporation
726 and sea-ice retreat. *Nature*, 509(7501), 479–482. <https://doi.org/10.1038/nature13259>
- 727 Bonne, J.-L., Masson-Delmotte, V., Cattani, O., Delmotte, M., Risi, C., Sodemann, H., & Steen-Larsen,
728 H. C. (2014). The isotopic composition of water vapour and precipitation in Ivittuut, southern
729 Greenland. *Atmospheric Chemistry and Physics*, 14(9), 4419–4439.
730 <https://doi.org/10.5194/acp-14-4419-2014>
- 731 Bonne, J.-L., Steen-Larsen, H. C., Risi, C., Werner, M., Sodemann, H., Lacour, J.-L., et al. (2015). The
732 summer 2012 Greenland heat wave: In situ and remote sensing observations of water vapor

- 733 isotopic composition during an atmospheric river event. *Journal of Geophysical Research:*
734 *Atmospheres*, 120(7), 2970–2989. <https://doi.org/10.1002/2014JD022602>
- 735 Bonne, J.-L., Behrens, M., Meyer, H., Kipfstuhl, S., Rabe, B., Schönike, L., et al. (2019). Resolving the
736 controls of water vapour isotopes in the Atlantic sector. *Nature Communications*, 10(1),
737 1632. <https://doi.org/10.1038/s41467-019-09242-6>
- 738 Bréant, C., Leroy-Dos Santos, C., Agosta, C., Casado, M., Fourré, E., Goursaud, S., et al. (2019). Coastal
739 water vapor isotopic composition driven by katabatic wind variability in summer at Dumont
740 d’Urville, coastal East Antarctica. *Earth and Planetary Science Letters*, 514, 37–47.
741 <https://doi.org/10.1016/j.epsl.2019.03.004>
- 742 Casado, M., Landais, A., Masson-Delmotte, V., Genthon, C., Kerstel, E., Kassi, S., et al. (2016).
743 Continuous measurements of isotopic composition of water vapour on the EastAntarctic
744 Plateau. *Atmospheric Chemistry and Physics*, 16(13), 8521–8538.
745 <https://doi.org/10.5194/acp-16-8521-2016>
- 746 Ciais, P., & Jouzel, J. (1994). Deuterium and oxygen 18 in precipitation: Isotopic model, including
747 mixed cloud processes. *Journal of Geophysical Research*, 99(D8), 16793.
748 <https://doi.org/10.1029/94JD00412>
- 749 Craig, H., & Gordon, L. I. (1965). Deuterium and oxygen 18 variations in the ocean and the marine
750 atmosphere.
- 751 Dahlke, S., & Maturilli, M. (2017). Contribution of Atmospheric Advection to the Amplified Winter
752 Warming in the Arctic North Atlantic Region. *Advances in Meteorology*, 2017, 1–8.
753 <https://doi.org/10.1155/2017/4928620>
- 754 Dahlke, S., Hughes, N. E., Wagner, P. M., Gerland, S., Wawrzyniak, T., Ivanov, B., & Maturilli, M.
755 (2020). The observed recent surface air temperature development across Svalbard and
756 concurring footprints in local sea ice cover. *International Journal of Climatology*, joc.6517.
757 <https://doi.org/10.1002/joc.6517>

- 758 Dansgaard, W. (1964). Stable isotopes in precipitation. *Tellus*, 16(4), 436–468.
759 <https://doi.org/10.1111/j.2153-3490.1964.tb00181.x>
- 760 Ding, Q., Schweiger, A., L'Heureux, M., Battisti, D. S., Po-Chedley, S., Johnson, N. C., et al. (2017).
761 Influence of high-latitude atmospheric circulation changes on summertime Arctic sea ice.
762 *Nature Climate Change*, 7(4), 289–295. <https://doi.org/10.1038/nclimate3241>
- 763 Divine, D. V., Isaksson, E., Pohjola, V., Meijer, H., van de Wal, R. S. W., Martma, T., et al. (2008).
764 Deuterium excess record from a small Arctic ice cap. *Journal of Geophysical Research*,
765 113(D19), D19104. <https://doi.org/10.1029/2008JD010076>
- 766 Dufour, A., Zolina, O., & Gulev, S. K. (2016). Atmospheric Moisture Transport to the Arctic:
767 Assessment of Reanalyses and Analysis of Transport Components. *Journal of Climate*, 29(14),
768 5061–5081. <https://doi.org/10.1175/JCLI-D-15-0559.1>
- 769 Dütsch, M., Pfahl, S., & Sodemann, H. (2017). The impact of nonequilibrium and equilibrium
770 fractionation on two different deuterium excess definitions. *Journal of Geophysical Research:*
771 *Atmospheres*, 122(23), 12–732.
- 772 Eckhardt, S., Hermansen, O., Grythe, H., Fiebig, M., Stebel, K., Cassiani, M., et al. (2013). The
773 influence of cruise ship emissions on air pollution in Svalbard - a harbinger of a more polluted
774 Arctic? *Atmospheric Chemistry and Physics*, 13(16), 8401–8409. [https://doi.org/10.5194/acp-](https://doi.org/10.5194/acp-13-8401-2013)
775 [13-8401-2013](https://doi.org/10.5194/acp-13-8401-2013)
- 776 Galewsky, J., Steen-Larsen, H. C., Field, R. D., Worden, J., Risi, C., & Schneider, M. (2016). Stable
777 isotopes in atmospheric water vapor and applications to the hydrologic cycle: ISOTOPES IN
778 THE ATMOSPHERIC WATER CYCLE. *Reviews of Geophysics*, 54(4), 809–865.
779 <https://doi.org/10.1002/2015RG000512>
- 780 Gjelten, H. M., Nordli, Ø., Isaksen, K., Førland, E. J., Sviashchennikov, P. N., Wyszynski, P., et al.
781 (2016). Air temperature variations and gradients along the coast and fjords of western
782 Spitsbergen. *Polar Research*, 35(1), 29878. <https://doi.org/10.3402/polar.v35.29878>

- 783 Goosse, H., Kay, J. E., Armour, K. C., Bodas-Salcedo, A., Chepfer, H., Docquier, D., et al. (2018).
784 Quantifying climate feedbacks in polar regions. *Nature Communications*, *9*(1), 1919.
785 <https://doi.org/10.1038/s41467-018-04173-0>
- 786 Hanssen-Bauer, I., & Førland, E. (1998). Long-term trends in precipitation and temperature in the
787 Norwegian Arctic: can they be explained by changes in atmospheric circulation patterns?
788 *Climate Research*, *10*, 143–153. <https://doi.org/10.3354/cr010143>
- 789 Hao, M., Luo, Y., Lin, Y., Zhao, Z., Wang, L., & Huang, J. (2019). Contribution of atmospheric moisture
790 transport to winter Arctic warming. *International Journal of Climatology*, *39*(5), 2697–2710.
791 <https://doi.org/10.1002/joc.5982>
- 792 Hendricks, M. B., DePaolo, D. J., & Cohen, R. C. (2000). Space and time variation of $\delta^{18}\text{O}$ and δD in
793 precipitation: Can paleotemperature be estimated from ice cores? *Global Biogeochemical*
794 *Cycles*, *14*(3), 851–861. <https://doi.org/10.1029/1999GB001198>
- 795 International Atomic Energy Agency. (2006). *Reference Sheet for International Measurement*
796 *Standards*. Retrieved from https://nucleus.iaea.org/rpst/documents/VSMOW_SLAP.pdf
- 797 Isaksen, K., Nordli, Ø., Førland, E. J., Łupikasza, E., Eastwood, S., & Niedźwiedź, T. (2016). Recent
798 warming on Spitsbergen-Influence of atmospheric circulation and sea ice cover. *Journal of*
799 *Geophysical Research: Atmospheres*, *121*(20), 11,913-11,931.
800 <https://doi.org/10.1002/2016JD025606>
- 801 Isaksson, E., Kohler, J., Pohjola, V., Moore, J., Igarashi, M., Karlöf, L., et al. (2005). Two ice-core $\delta^{18}\text{O}$
802 records from Svalbard illustrating climate and sea-ice variability over the last 400 years. *The*
803 *Holocene*, *15*(4), 501–509. <https://doi.org/10.1191/0959683605hl820rp>
- 804 Jouzel, J., Delaygue, G., Landais, A., Masson-Delmotte, V., Risi, C., & Vimeux, F. (2013). Water
805 isotopes as tools to document oceanic sources of precipitation: Water Isotopes and
806 Precipitation Origin. *Water Resources Research*, *49*(11), 7469–7486.
807 <https://doi.org/10.1002/2013WR013508>

- 808 Jouzel, Jean, & Merlivat, L. (1984). Deuterium and oxygen 18 in precipitation: Modeling of the
809 isotopic effects during snow formation. *Journal of Geophysical Research: Atmospheres*,
810 *89*(D7), 11749–11757.
- 811 Kopec, B. G., Lauder, A. M., Posmentier, E. S., & Feng, X. (2014). The diel cycle of water vapor in west
812 Greenland: west Greenland diel cycle of water vapor. *Journal of Geophysical Research:*
813 *Atmospheres*, *119*(15), 9386–9399. <https://doi.org/10.1002/2014JD021859>
- 814 Kopec, B. G., Feng, X., Posmentier, E. S., & Sonder, L. J. (2019). Seasonal Deuterium Excess Variations
815 of Precipitation at Summit, Greenland, and their Climatological Significance. *Journal of*
816 *Geophysical Research: Atmospheres*, *124*(1), 72–91. <https://doi.org/10.1029/2018JD028750>
- 817 Kurita, N. (2003). Relationship between the variation of isotopic ratios and the source of summer
818 precipitation in eastern Siberia. *Journal of Geophysical Research*, *108*(D11), 4339.
819 <https://doi.org/10.1029/2001JD001359>
- 820 Liu, C., & Barnes, E. A. (2015). Extreme moisture transport into the Arctic linked to Rossby wave
821 breaking: extreme moisture flux and wave breaking. *Journal of Geophysical Research:*
822 *Atmospheres*, *120*(9), 3774–3788. <https://doi.org/10.1002/2014JD022796>
- 823 Majoube, M. (1971). Fractionnement en $\delta^{18}\text{O}$ entre la glace et la vapeur d'eau. *Journal de Chimie*
824 *Physique*, *68*, 625–636.
- 825 Masson-Delmotte, V., Hou, S., Ekaykin, A., Jouzel, J., Aristarain, A., Bernardo, R. T., et al. (2008). A
826 Review of Antarctic Surface Snow Isotopic Composition: Observations, Atmospheric
827 Circulation, and Isotopic Modeling. *Journal of Climate*, *21*(13), 3359–3387.
828 <https://doi.org/10.1175/2007JCLI2139.1>
- 829 Maturilli, M. (2018). High resolution radiosonde measurements from station Ny-Ålesund (2017-12).
830 PANGAEA. <https://doi.org/10.1594/PANGAEA.886871>
- 831 Maturilli, M. (2020a). Basic and other measurements of radiation at station Ny-Ålesund (2020-04).
832 PANGAEA. <https://doi.org/10.1594/PANGAEA.917580>

- 833 Maturilli, M. (2020b). High resolution radiosonde measurements from station Ny-Ålesund (2017-04
834 et seq). PANGAEA. <https://doi.org/10.1594/PANGAEA.914973>
- 835 Maturilli, M., & Ebell, K. (2018). Twenty-five years of cloud base height measurements by ceilometer
836 in Ny-Ålesund, Svalbard. *Earth System Science Data*, *10*(3), 1451–1456.
837 <https://doi.org/10.5194/essd-10-1451-2018>
- 838 Maturilli, M., & Kayser, M. (2017). Arctic warming, moisture increase and circulation changes
839 observed in the Ny-Ålesund homogenized radiosonde record. *Theoretical and Applied*
840 *Climatology*, *130*(1–2), 1–17. <https://doi.org/10.1007/s00704-016-1864-0>
- 841 Meredith, M., Sommerkorn, M., Cassota, S., Derksen, C., Ekaykin, A., Hollowed, A., et al. (2019). *IPCC*
842 *Special Report on the Ocean and Cryosphere in a Changing Climate: Chapter 3: Polar Regions.*
- 843 Merlivat, L., & Nief, G. (1967). Fractionnement isotopique lors des changements d'état solide-vapeur
844 et liquide-vapeur de l'eau à des températures inférieures à 0°C. *Tellus*, *19*(1), 122–127.
845 <https://doi.org/10.1111/j.2153-3490.1967.tb01465.x>
- 846 Merlivat, Liliane, & Jouzel, J. (1979). Global climatic interpretation of the deuterium-oxygen 18
847 relationship for precipitation. *Journal of Geophysical Research*, *84*(C8), 5029.
848 <https://doi.org/10.1029/JC084iC08p05029>
- 849 Naakka, T., Nygård, T., Vihma, T., Sedlar, J., & Graversen, R. (2019). Atmospheric moisture transport
850 between mid-latitudes and the Arctic: Regional, seasonal and vertical distributions.
851 *International Journal of Climatology*, *39*(6), 2862–2879. <https://doi.org/10.1002/joc.5988>
- 852 Ngan, F., Loughner, C. P., & Stein, A. (2019). The evaluation of mixing methods in HYSPLIT using
853 measurements from controlled tracer experiments. *Atmospheric Environment*, *219*, 117043.
- 854 Nomokonova, T., Ebell, K., Löhnert, U., Maturilli, M., & Ritter, C. (2020). The influence of water vapor
855 anomalies on clouds and their radiative effect at Ny-Ålesund. *Atmospheric*
856 *Chemistry and Physics*, *20*(8), 5157–5173. <https://doi.org/10.5194/acp-20-5157-2020>
- 857 Opel, T., Fritzsche, D., Meyer, H., Schütt, R., Weiler, K., Ruth, U., et al. (2009). 115 year ice-core data
858 from Akademii Nauk ice cap, Severnaya Zemlya: high-resolution record of Eurasian Arctic

- 859 climate change. *Journal of Glaciology*, 55(189), 21–31.
860 <https://doi.org/10.3189/002214309788609029>
- 861 Overland, J. E., & Wang, M. (2018). Arctic-midlatitude weather linkages in North America. *Polar*
862 *Science*, 16, 1–9. <https://doi.org/10.1016/j.polar.2018.02.001>
- 863 Papritz, L., & Sodemann, H. (2018). Characterizing the Local and Intense Water Cycle during a Cold Air
864 Outbreak in the Nordic Seas. *Monthly Weather Review*, 146(11), 3567–3588.
865 <https://doi.org/10.1175/MWR-D-18-0172.1>
- 866 Picarro Inc. (2009). *L1102-i Analyzer User's Guide*. Sunnyvale, CA, USA: Picarro Inc., Sunnyvale, CA,
867 USA. Retrieved from <https://www.picarro.com/support/documents>
- 868 Picarro Inc. (2016). *L2130-i Analyzer User's Guide*. Sunnyvale, CA, USA: Picarro Inc., Sunnyvale, CA,
869 USA. Retrieved from <https://www.picarro.com/support/documents>
- 870 Rayleigh, Lord. (1902). LIX. On the distillation of binary mixtures. *The London, Edinburgh, and Dublin*
871 *Philosophical Magazine and Journal of Science*, 4(23), 521–537.
- 872 Rinke, A., Maturilli, M., Graham, R. M., Matthes, H., Handorf, D., Cohen, L., et al. (2017). Extreme
873 cyclone events in the Arctic: Wintertime variability and trends. *Environmental Research*
874 *Letters*, 12(9), 094006. <https://doi.org/10.1088/1748-9326/aa7def>
- 875 Rinke, A., Segger, B., Crewell, S., Maturilli, M., Naakka, T., Nygård, T., et al. (2019). Trends of
876 Vertically Integrated Water Vapor over the Arctic during 1979–2016: Consistent Moistening
877 All Over? *Journal of Climate*, 32(18), 6097–6116. <https://doi.org/10.1175/JCLI-D-19-0092.1>
- 878 Risi, C., Bony, S., & Vimeux, F. (2008). Influence of convective processes on the isotopic composition
879 ($\delta^{18}\text{O}$ and δD) of precipitation and water vapor in the tropics: 2. Physical interpretation of
880 the amount effect. *Journal of Geophysical Research: Atmospheres*, 113(D19).
- 881 Risi, C., Bony, S., Vimeux, F., Chong, M., & Descroix, L. (2010). Evolution of the stable water isotopic
882 composition of the rain sampled along Sahelian squall lines. *Quarterly Journal of the Royal*
883 *Meteorological Society*, 136(S1), 227–242.

- 884 Risi, C., Bony, S., Vimeux, F., & Jouzel, J. (2010). Water-stable isotopes in the LMDZ4 general
885 circulation model: Model evaluation for present-day and past climates and applications to
886 climatic interpretations of tropical isotopic records. *Journal of Geophysical Research*,
887 *115*(D12), D12118. <https://doi.org/10.1029/2009JD013255>
- 888 Ritter, F., Steen-Larsen, H. C., Werner, M., Masson-Delmotte, V., Orsi, A., Behrens, M., et al. (2016).
889 Isotopic exchange on the diurnal scale between near-surface snow and lower atmospheric
890 water vapor at Kohnen station, East Antarctica. *The Cryosphere*, *10*(4), 1647–1663.
891 <https://doi.org/10.5194/tc-10-1647-2016>
- 892 Screen, J. A., & Simmonds, I. (2010). The central role of diminishing sea ice in recent Arctic
893 temperature amplification. *Nature*, *464*(7293), 1334–1337.
894 <https://doi.org/10.1038/nature09051>
- 895 Smith, R. B., & Evans, J. P. (2007). Orographic Precipitation and Water Vapor Fractionation over the
896 Southern Andes. *Journal of Hydrometeorology*, *8*(1), 3–19.
897 <https://doi.org/10.1175/JHM555.1>
- 898 Sodemann, H., Schwierz, C., & Wernli, H. (2008). Interannual variability of Greenland winter
899 precipitation sources: Lagrangian moisture diagnostic and North Atlantic Oscillation
900 influence. *Journal of Geophysical Research*, *113*(D3), D03107.
901 <https://doi.org/10.1029/2007JD008503>
- 902 Sodemann, Harald, Aemisegger, F., Pfahl, S., Bitter, M., Corsmeier, U., Feuerle, T., et al. (2017). The
903 stable isotopic composition of water vapour above Corsica during the HyMeX SOP1
904 campaign: insight into vertical mixing processes from lower-tropospheric survey flights.
905 *Atmospheric Chemistry and Physics*, *17*(9), 6125–6151.
- 906 Steen-Larsen, H. C., Masson-Delmotte, V., Sjolte, J., Johnsen, S. J., Vinther, B. M., Bréon, F.-M., et al.
907 (2011). Understanding the climatic signal in the water stable isotope records from the NEEM
908 shallow firn/ice cores in northwest Greenland. *Journal of Geophysical Research*, *116*(D6),
909 D06108. <https://doi.org/10.1029/2010JD014311>

- 910 Steen-Larsen, H. C., Johnsen, S. J., Masson-Delmotte, V., Stenni, B., Risi, C., Sodemann, H., et al.
911 (2013). Continuous monitoring of summer surface water vapor isotopic composition above
912 the Greenland Ice Sheet. *Atmospheric Chemistry and Physics*, 13(9), 4815–4828.
913 <https://doi.org/10.5194/acp-13-4815-2013>
- 914 Steen-Larsen, H. C., Masson-Delmotte, V., Hirabayashi, M., Winkler, R., Satow, K., Prié, F., et al.
915 (2014). What controls the isotopic composition of Greenland surface snow? *Climate of the*
916 *Past*, 10(1), 377–392. <https://doi.org/10.5194/cp-10-377-2014>
- 917 Steen-Larsen, H. C., Sveinbjörnsdóttir, A. E., Jonsson, Th., Ritter, F., Bonne, J.-L., Masson-Delmotte,
918 V., et al. (2015). Moisture sources and synoptic to seasonal variability of North Atlantic water
919 vapor isotopic composition: north Atlantic water vapor isotopes. *Journal of Geophysical*
920 *Research: Atmospheres*, 120(12), 5757–5774. <https://doi.org/10.1002/2015JD023234>
- 921 Steen-Larsen, H. C., Risi, C., Werner, M., Yoshimura, K., & Masson-Delmotte, V. (2017). Evaluating the
922 skills of isotope-enabled general circulation models against in situ atmospheric water vapor
923 isotope observations: Evaluating Isotope-Enabled GCMs. *Journal of Geophysical Research:*
924 *Atmospheres*, 122(1), 246–263. <https://doi.org/10.1002/2016JD025443>
- 925 Stein, A. F., Draxler, R. R., Rolph, G. D., Stunder, B. J. B., Cohen, M. D., & Ngan, F. (2015). NOAA's
926 HYSPLIT Atmospheric Transport and Dispersion Modeling System. *Bulletin of the American*
927 *Meteorological Society*, 96(12), 2059–2077. <https://doi.org/10.1175/BAMS-D-14-00110.1>
- 928 Stern, L. A., & Blisniuk, P. M. (2002). Stable isotope composition of precipitation across the southern
929 Patagonian Andes: stable isotope composition of precipitation. *Journal of Geophysical*
930 *Research: Atmospheres*, 107(D23), ACL 3-1-ACL 3-14. <https://doi.org/10.1029/2002JD002509>
- 931 Stohl, A., Forster, C., Frank, A., Seibert, P., & Wotawa, G. (2005). The Lagrangian particle dispersion
932 model FLEXPART version 6.2. *Atmos. Chem. Phys.*, 14.
- 933 Touzeau, A., Landais, A., Stenni, B., Uemura, R., Fukui, K., Fujita, S., et al. (2016). Acquisition of
934 isotopic composition for surface snow in East Antarctica and the links to climatic parameters.
935 *The Cryosphere*, 17.

- 936 Tremoy, G., Vimeux, F., Cattani, O., Mayaki, S., Souley, I., & Favreau, G. (2011). Measurements of
937 water vapor isotope ratios with wavelength-scanned cavity ring-down spectroscopy
938 technology: new insights and important caveats for deuterium excess measurements in
939 tropical areas in comparison with isotope-ratio mass spectrometry: Measuring tropical water
940 vapor isotope ratios using WS-CRDS. *Rapid Communications in Mass Spectrometry*, *25*(23),
941 3469–3480. <https://doi.org/10.1002/rcm.5252>
- 942 Uemura, R., Masson-Delmotte, V., Jouzel, J., Landais, A., Motoyama, H., & Stenni, B. (2012). Ranges
943 of moisture-source temperature estimated from Antarctic ice cores stable isotope records
944 over glacial–interglacial cycles. *Climate of the Past*, *8*(3), 1109–1125.
945 <https://doi.org/10.5194/cp-8-1109-2012>
- 946 Vázquez, M., Nieto, R., Drumond, A., & Gimeno, L. (2016). Moisture transport into the Arctic: Source-
947 receptor relationships and the roles of atmospheric circulation and evaporation. *Journal of*
948 *Geophysical Research: Atmospheres*, *121*(22), 13,493–13,509.
949 <https://doi.org/10.1002/2016JD025400>
- 950 Walsh, J. E., Fetterer, F., Scott Stewart, J., & Chapman, W. L. (2017). A database for depicting Arctic
951 sea ice variations back to 1850. *Geographical Review*, *107*(1), 89–107.
952 <https://doi.org/10.1111/j.1931-0846.2016.12195.x>
- 953 Werner, M., Langebroek, P. M., Carlsen, T., Herold, M., & Lohmann, G. (2011). Stable water isotopes
954 in the ECHAM5 general circulation model: Toward high-resolution isotope modeling on a
955 global scale. *Journal of Geophysical Research*, *116*(D15), D15109.
956 <https://doi.org/10.1029/2011JD015681>
- 957 Woods, C., Caballero, R., & Svensson, G. (2013). Large-scale circulation associated with moisture
958 intrusions into the Arctic during winter. *Geophysical Research Letters*, *40*(17), 4717–4721.
959 <https://doi.org/10.1002/grl.50912>
- 960 Zhang, X., Walsh, J. E., & Zhang, J. (2004). Climatology and Interannual Variability of Arctic Cyclone
961 Activity: 1948–2002. *JOURNAL OF CLIMATE*, *17*, 19.

962

963